An Interactive Operating Demand Response Approach for Hybrid Power Systems Integrating Renewable Energy Sources

Abhishek Saxena, *Student Member*, *IEEE*, and Ravi Shankar

***Abstract*—The increased deployment of renewable energy in existing power networks has jeopardized rotational inertia, resulting in system degradation and instability. To address the issue, this paper proposes a demand response strategy for ensuring the future reliability of the electrical power system. In addition, a modified fuzzy logic control topology-based two-degree-of-freedom (fractional order proportional integral)-tilt derivative controller is designed to regulate the frequency within a demand response framework of a hybrid two-area deregulated power system. The test system includes thermal power plants, renewable energy sources (such as wind, parabolic trough solar thermal plant, biogas), and electric vehicle assets. To adaptively tune the controller's coefficients, a quasi-opposition-based harris hawks optimization (QOHHO) algorithm is developed. The effectiveness of this algorithm is compared to other optimization algorithms, and the stability of the system is evaluated. The results demonstrate that the designed control algorithm significantly enhances system frequency stability in various scenarios, including uncertainties, physical constraints, and high penetration of renewables, compared to existing work. Additionally, an experimental assessment through OPAL-RT is conducted to verify the practicality of the proposed strategy, considering source and load intermittencies.**

***Index Terms*—Area control error, demand response, energy storage, vertically integrated utility.**

I. Introduction

A. General

Over the past few years, there has been growing interest in improving frequency regulation (FR) services in power systems, primarily due to the increasing integration of renewable energy sources (RES) like solar and wind into the electrical power grid. The intermittent nature of these RES introduces considerable challenges in maintaining a harmonious balance between electricity generation and demand, resulting in frequency fluctuations across the power grid [1]. In addition, global energy consumption has witnessed a surge because of the continuous growth of the world population and the pursuit of economic development. Consequently, there is a growing recognition of the urgent necessity for sustainable energy practices [2]. While fossil fuels have long dominated the energy landscape, there is a progressive shift towards cleaner and greener energy sources driven by concerns about climate change, air pollution, and the finite nature of fossil fuel reserves [3]. FR is crucial for maintaining grid stability, as even small deviations from the nominal frequency can have detrimental effects on the entire power system [4]. To mitigate the challenges of intermittent RES and ensure future grid stability, effectively implementing demand response (DR) strategies to reduce peak demand is a prudent alternative. Furthermore, researchers are actively exploring DR strategies for enhancing FR services in power systems because of their potential to effectively address the challenges associated with RES penetration [5]. By harnessing the benefits of DR, the power grid can attain a high level of resilience and adaptability, paving the way for a sustainable energy future.

B. Literature Review

There are several control approaches for FR analysis, and performance assessment of distinct control schemes for grid stabilization have been noted e.g., extra degrees of emancipation control scheme [6], [7], disturbance observer assisted fractional higher-degree-of-freedom [8], H-infinity [9], and fuzzy logic control [10], [11]. On the other hand, most of these strategies are intricate, needing more configurable parameters, lengthier computation time, etc. As a result, using a resilient fuzzy control strategy based on a feedback topology is recommended. This method offers significant benefits as it remains independent of any particular model, effectively rectifying existing shortcomings while preserving the dynamic performance of the deregulated power system. Also electrical grids are progressively moving

Received: September 12, 2023
Accepted: November 1, 2023
Published Online: May 1, 2024
Abhishek Saxena (corresponding author) is with the Department of Electrical Engineering, National Institute of Technology Patna, India (abhishek.ee18@nitp.ac.in).
DOI: 10.23919/PCMP.2023.000282

towards deregulation, creating a competitive energy market. In a deregulated environment, distribution companies (Disco) may contact directly with generation companies (Gencos) at distinct locations [12].

RES and bio-renewable sources have excellent qualities since they are clean, carbon-free, and environmentally sustainable [13], [14]. An elementary model of solar thermal for FR service is reported in [15], while an attempt to integrate solar and thermal power generation is illustrated in [16]. Substantial inclusion of RES, especially solar and wind cogeneration due to their intermittent nature, may result in significant issues, including distribution voltage hikes and frequency imbalances [17]. A battery energy storage system (BESS) may be an alternative to such impediments. However, owing to the high price of BESS, using electric vehicles may be a practical approach [17], [18]. The increasing popularity of two-way communication has made DR a preferred solution for power system challenges [19], [20]. Appliances such as air conditioners, geysers, refrigerators, and other low-priority loads can take part in the DR mechanism. However, the previous frequency control methods may not be sufficient to maintain uniform frequency in the future, while traditional frequency regulation schemes [21] combined with DR, can help improve frequency stability [22], [23].

Optimizing controller parameters is essential for effective performance. In the automatic generation control (AGC) study, several optimization techniques are used, such as salp swarm algorithm (SSA) [24], whale optimization algorithm (WOA) [25], particle swarm optimization (PSO) [26], ant lion optimizer (ALO) [27], grey wolf optimizer (GWO) [28], and teaching learning-based optimization (TLBO) [29]. To obtain the appropriate coefficients for secondary controllers, a modified quasi-opposition-based harris hawks optimization (QOHHO) approach is developed using the quasi-opposition-based learning (QOBL) method [30] in harris hawks optimization (HHO) [31].

C. Research Gap and Motivation

Based on existing literature, few have implemented DR share [22], [32]–[35] in FR modeling for improved system performance. Reference [35] offers a framework for combining multi-machine models analytically with DR, while [33] shows the impact of DR regulatory support on frequency deviation characteristics. References [23], [33] use classical generating units. In the few studies available for grid frequency stabilization with DR [36], RES assimilation is introduced and examined without energy storage (ES) technology. Reference [35], [37] include BES and DR, whereas [38], [39] do not discuss DR schemes for power grid frequency control. The efficiency of DR control in frequency stabilization has been highlighted in numerous studies [22], [32]–[36], but [33] has yet to investigate the robustness of the additional and DR control approach for grid physical constraints. The potential impact of communication delay on the DR method is an intriguing aspect that references [22], [23] could further explore to uncover valuable insights. While some studies have investigated the use of DR for frequency stabilization problems in the presence of RES penetration [40], real-time assessment remains largely unexplored. The influence of DR for grid frequency stabilization with communication lag, considering the intermittent behavior of RES and system non-linear constraints, has yet to be investigated. Furthermore, a hardware-in-the-loop (HIL) validation to assess the influence of DR for frequency stabilization needs to be examined.

The motivation for examining DR impact on frequency stabilization with the intermittent characteristic of renewable power sources are as follows:

1) DR allows customers to contribute to grid reliability by lowering or changing their peak hour electrical consumption in the light of time-based rates or other economic assistance.

2) Less demand provides less strain on energy transition and distribution networks, reducing their loss rate, while demand reduction also increases grid reliability.

3) To improve frequency regulation, utilities are attempting to include some DR capabilities in addition to load shifting, shaping, and geographic network congestion.

4) The DR strategy is a dynamic and adaptable technique for maintaining system equilibrium when combining intermittent energy sources into the power grid.

The main contributions of this paper are:

1) A hierarchical frequency regulation incorporating DR is proposed, providing valuable insights and a thorough analysis of system performance. The influence of DR control on the transient characteristics of a deregulated power network is explored. This is especially important because of the intermittency of RES.

2) To analyze the system dynamic response with the source and load intermittencies, a QOHHO tuned modified fuzzy logic control topology-based two-degree-of-freedom (fractional order proportional integral)-tilt derivative controller named modified TDOF is designed. Its efficacy in minimizing fluctuations in the frequency and tie-line power variations is demonstrated.

3) The stability of the studied deregulated power network is evaluated, followed by analysis for randomly varying demand. A comparison with the existing methods on a similar podium is also illustrated.

4) The practicality of the suggested control mechanism is verified with an HIL study using OPAL-RT. The findings offer new perspectives on integrating DR into hierarchical FR for more efficient and stable power networks.

The rest of the paper is organized as follows. The frequency regulation mechanism with DR that has been investigated is presented in Section II, while Sections III

and IV briefly overview the examined system modeling and dynamic system performance. Sections V and VI furnish an outline of the implemented controller, suggested algorithm, and problem formulation. Deregulated scenario and simulation findings are reported in Sections VII and VIII, respectively. Finally, the overall work is concluded in Section IX.

II. Methodology

DR is a low-cost effort that allows electricity companies to temporarily disconnect non-essential loads from the grid during periods of excessive load demand. It is a pre-negotiated contract between the utility and its subscribers. FR's three types of DR mechanisms are centrally monitored, de-centralized, and hybridized. In this study, a hybridized DR mechanism is constructed with the best aspects of centralized and decentralized. The resulting hybrid DR scheme is depicted in Fig. 1.

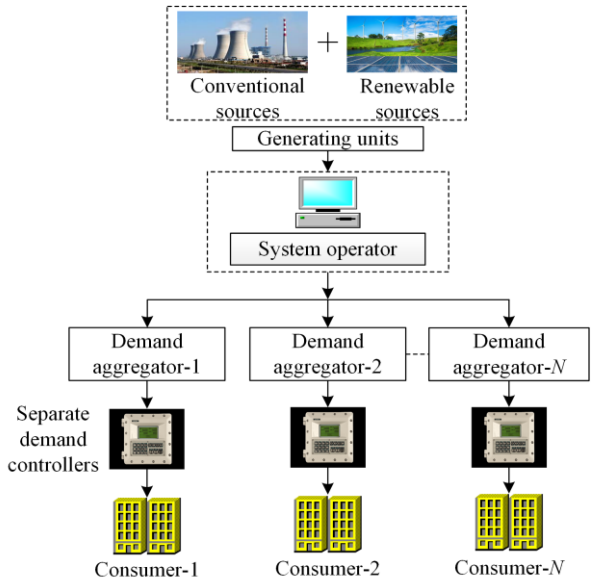

Fig. 1. Framework of hybrid DR scheme.

A. Demand Response Contrivance for Enhanced FR

Utility centers carry out demand response events in two ways: direct load inspection and time-based program rates. Previously, load centers controlled subscriber usage remotely during high burdens, but dynamic rates use varying power prices to encourage public participation. A direct load monitoring approach for frequency stabilization is proposed in this paper. The control scheme in the DR path evaluates the base frequency to determine whether or not to conduct primary level (PL) when there is an under-frequency disruption. If the frequency stabilizes, the controller chooses subsidiary level (SL) inclusion to bring it closer to the acceptable boundaries.

B. Empowering Energy Efficiency: Transformative Potential of Demand Aggregation

In the electricity market, aggregators serve as a bridge between utility companies and their consumers. Each aggregator focuses on a particular area to ensure efficient monitoring of the DR power market's specific types of load demand. As intermediaries, aggregators work closely with customers, skillfully negotiating incentives for shedding negligible loads. Thus, it is worth considering aggregators as participants in the market.

C. Customized Demand Controllers Functioning

When a region's frequency f drops below the critical frequency f_{cri}, the controller deactivates trivial loads to prevent the frequency deviation from becoming too severe. If the nadir frequency is monitored, the system is delayed by T_{delay} to safeguard the devices. The control section will turn on the DR load again after T_{delay} has completed and the frequency f exceeds the critical frequency f_{cri}. The high-frequency variations $f_{\text{M}k}$ and T_{delay} in both regions are considered to be 0.5 Hz and 10 s in the studied system.

D. Characteristics of the Control Center

The control center marks an area's maximum frequency deviation range to ensure considerably better frequency response characteristics. In the past, most DR schemes only relied on frequency deviation, whereas a more productive method is proposed here, one which considers regional swing in frequency and power exchange to ameliorate the system's dynamic response. The amount of demand participating in DR that can be switched off can be given as [22].

$$P_{\text{DR}k}=\begin{cases}-P_{\text{DRM}k}, & \Delta f_k>\Delta f_{\text{M}k}\\ D_{\text{DR}k}\Delta f_k+T_{\text{DR}k}\sum_{l\neq k}\Delta P_{\text{tie},kl}, & -\Delta f_{\text{M}k}\leqslant\Delta f_k\leqslant\Delta f_{\text{M}k}\\ P_{\text{DRM}k}, & \Delta f_k<-\Delta f_{\text{M}k}\end{cases} \tag{1}$$

where $P_{\text{DRM}k}$ is the maximum available load that participates in DR, and it is taken at 0.1 p.u., i.e., 10% DR support $D_{\text{DR}k}$ and $T_{\text{DR}k}$ are the DR frequency alteration and a tie-line coefficient for area, respectively. $T_{\text{DR}k}$ is to be optimized and $D_{\text{DR}k}$ is fixed and computed as [33]:

$$D_{\text{DR}k}=\frac{P_{\text{DRM}k}}{\Delta f_{\text{M}k}} \tag{2}$$

III. Investigated System Modelling

All investigations in this study are carried out on a similar two-area system in a bilateral scenario. Each area comprises RES such as parabolic trough solar thermal plant (PTST), wind turbine, and bio-gas plant with generation rate constraints (GRC) of 20% per minute, i.e., 0.0033 p.u./s in conjunction with the thermal unit considering governor dead band (GDB) ($N_1=0.8, N_2=-0.2$ Pi), GRC = 0.005 s, and boiler

dynamics (BD) with a time delay of 0.1 s. EVs, a new energy storage system, are appended in both areas to alleviate the disparity during contract violations. The test system's dynamic behavior is examined against 1% step disturbance. The schematic layout of the investigated integrated grid system is presented in Fig. 2. Each area is assumed to have a nominal generating capability of 2000 MW, and 200 MW is the optimal threshold for tie-lines ultimate power exchange efficiency. The two regions are identical, and the ACE participation factors (APF) in each area for thermal, biogas, PTST, and EV are assumed to be 0.4, 0.3, 0.2, and 0.1, respectively. Therefore, after multiplying the base load of 2000 MW by APF, the installed ratings of thermal, biogas, PTST, and EV are 800 MW, 600 MW, 400 MW, and 200 MW, respectively. Additionally, wind power generation with an installed rating of 21.80 MW is integrated into both test areas. The power generating units of the evaluated system are summarized below.

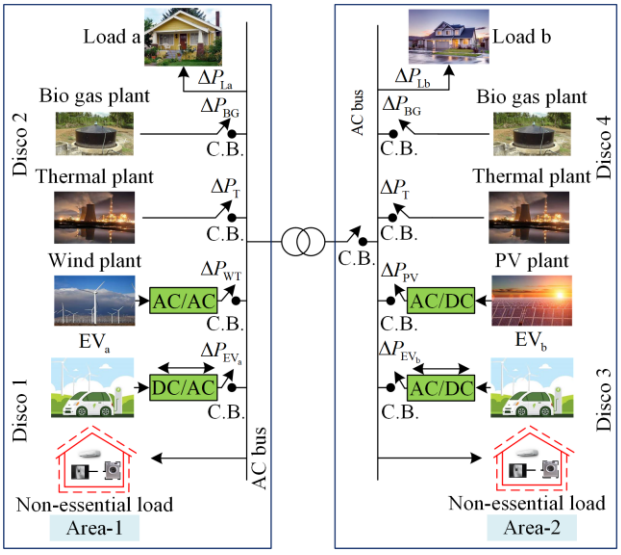

Fig. 2. Configuration of the interconnected two-area restructured power system.

A. Thermal Plant

The thermal plant comprises a governor and a reheat turbine. The physical constraints such as GDB and GRC of 3% per minute and BD are included for the actual examination with a time delay of 0.1 s. Figure 3 illustrates the expression of the linearized thermal power plant's transfer function model, and incorporates the governor, turbine, and system physical non-linearities [6].

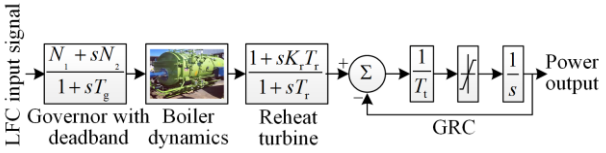

Fig. 3. Thermal plant with reheat turbine and non-linearities.

B. Bio-gas Power Unit

Biogas extracted from anaerobic digestion can be favorably used for power generation. The linear transfer function visualization of the biogas power plant [19] involving the governor, inlet valve, fuel system, and biogas turbine is approximated in Fig. 4.

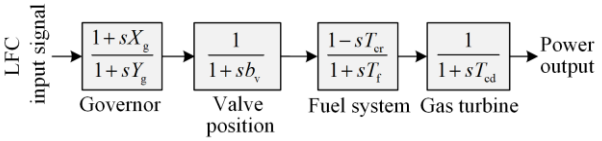

Fig. 4. Bio-gas power generating unit.

C. Wind Farm Power Generation

In recent decades, wind farms have produced a substantial rise in energy production. The mechanical power output [19] of the captured wind energy can be mathematically represented as:

$$P_{WF} = 0.5\rho A_R C_P(\lambda,\beta)V_W^3 \tag{3}$$

where ρ represents the density of air in kilograms per cubic meter; A_R refers to the swept area of the blade; $C_P(\lambda,\beta)$ denotes the power transmission coefficient; λ represents the tip speed ratio; β corresponds to the pitch angle of the blade; and V_W signifies the wind speed. Theoretical estimates suggest that doubling wind speed boosts wind power potential by a factor of eight. Figure 5 depicts the wind turbine layout.

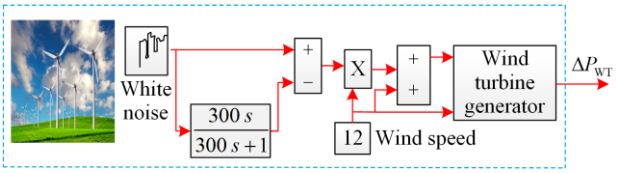

Fig. 5. Wind farm model.

D. Parabolic Trough Solar Thermal Plant

A parabolic trough is one category of solar thermal collector precisely straight in one dimension and parabolic in the other two. Under a parabolic configuration, troughs may emphasize the sun 30 to 100 times its intensity. The parabolic trough solar thermal (PTST) [15] technology uses the solar rays arriving on a solar collector that impels mirrors to focus solar rays on the receiver that converts them into heat. As a result, steam transforms mechanical energy, which is then used to power a turbine generator, generating usable electrical energy. It is possible to approximate the transfer function of the solar field collector as [15]:

$$G(s) = \frac{K_s}{1+sT_s} \tag{4}$$

where K_s and T_s are the respective gain and time constant of the solar field collector. Also, the linearized transfer function of the PTST governor and turbine are as follows:

$$G_{gst}(s) = \frac{1}{1+sT_{gst}} \tag{5}$$

$$G_{tst}(s) = \frac{1}{1+sT_{tst}} \tag{6}$$

where T_{gst} and T_{tst} are the PTST governor and turbine time constants respectively.

E. Electric Vehicles

Electric vehicles present a feasible solution for meeting uncontracted electricity demands. Figure 6 (a) illustrates the idle mode of electric vehicles. The kinetic energy gain of EVs denoted as K_{EV}, can be determined based on the state of charge (SOC) [17]. EVs do not fully engage in FR when the SOC falls in the transient phase within the range of SOC_a and SOC_b. EV maximum and minimum output power reserves can be specified by ΔP_{EV}^{max} and ΔP_{EV}^{min} respectively as [18]:

$$\Delta P_{max}^{EV} = +\left[\frac{1}{N_{EV}} \times \Delta P_{EV}\right] \tag{7}$$

$$\Delta P_{min}^{EV} = -\left[\frac{1}{N_{EV}} \times \Delta P_{EV}\right] \tag{8}$$

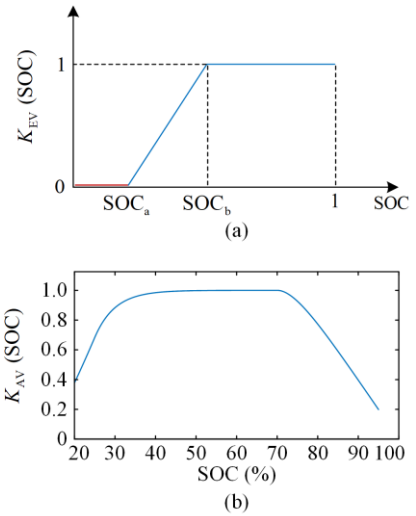

Fig. 6. Characteristic curves. (a) K_{EV} versus SOC in idle mode case. (b) K_{AV} versus SOC.

where N_{EV} indicates the number of connected EVs and ΔP_{EV} shows EV generation change incrementally. The electric vehicle charging/discharging capacity is estimated at 5 kW, potentially increasing to 50 kW [17]. EVs will not support frequency change if the SOC is less than the minimum needed SOC_a. If the SOC is between 50% and 70% and the K_{EV} value is 1 [17]. The characteristic of average gain K_{AV} versus SOC is shown in Fig. 6 (b). According to ACE, EV power output can be given as [18]:

$$\Delta P_{EV} = \begin{cases} K_{EV}\text{ACE}, & |K_{EV}\text{ACE}| \leqslant \Delta P^{max} \\ \Delta P^{max}, & |K_{EV}\text{ACE}| > \Delta P^{max} \\ \Delta P^{min}, & |K_{EV}\text{ACE}| < \Delta P^{min} \end{cases} \tag{9}$$

The EV does not compete in frequency alteration phenomena when its power output is out of range. After injecting power into the grid, the SOC of an EV may change, and the updated SOC can be determined through calculation as:

$$SOC_{new} = SOC_{old} - \left(\frac{\Delta E}{E_{rated}}\right) \tag{10}$$

where SOC_{new} represents the SOC of a battery after the injection of energy ΔE; whereas SOC_{old} corresponds to the residual SOC value before the energy injection; E_{rated} represents the rated value of EV, and the injectable energy ΔE is given by:

$$\Delta E = P_{inj}\, \Delta t \tag{11}$$

where P_{inj} is the injected power during time Δt. The linearized model of an EV is shown in Fig. 7, while Fig. 8 shows the analysed power system transfer function model for frequency stabilization considering DR influence.

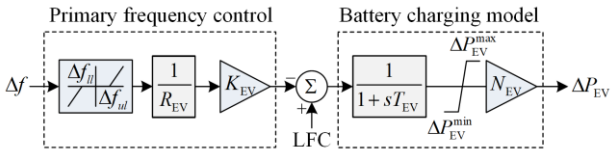

Fig. 7. Linearized control model of an electric vehicle.

IV. Assessing Power System Dynamics with DR

A. Characterization of Steady State Error

The frequency control depicted in Fig. 8 is a rapid response mechanism inherent to the power system. However, more effort is needed to eliminate frequency variation entirely in a steady-state scenario. Therefore, supplementary secondary regulation (SR) [33] is necessary for effective control operation. A DR [35] has been incorporated into the test system configuration to enhance the system's dynamic behavior further. Consequently, it is essential to evaluate the significance of DR on the system's behavior in stable conditions. In the case of the two-area hybrid system under examination, the frequency variation of the system is expressed as:

$$\Delta f_k(s) = \frac{\left[\begin{matrix} H_{\Theta,k}(s)\Delta P_{\Theta,k}(s) - \Delta P_{d,k}(s) + G_k(s)\Delta P_{DR,k}(s) \pm \\ \Delta P_{EV}(s) - \Delta P_{tie,kl}(s) \end{matrix}\right]}{2H_k s + D_k + (H_{\Theta,k}(s)/R_k)} \tag{12}$$

where $\Delta P_{\Theta,k}(s) = \Delta P_{th,k} + \Delta P_{re,k}$ is the sum of the thermal and RE (WT, PTSTP, and biogas) regulatory power; while $H_{\Theta,k}(s) = H_{th,k}(s) + H_{re,k}(s)$ is the equivalent illustration of a generator's governor and turbine; $\Delta P_{DR,k}(s)$ is DR's overall regulation and $\Delta P_{EV}(s)$ is the injected/absorbed power by the EV. The fraction of tie-line power can be given as:

$$\Delta P_{tie,kl}(s) = \frac{2\pi}{s} T_{12}[\Delta f_k(s) - \Delta f_l(s)], k \neq l \tag{13}$$

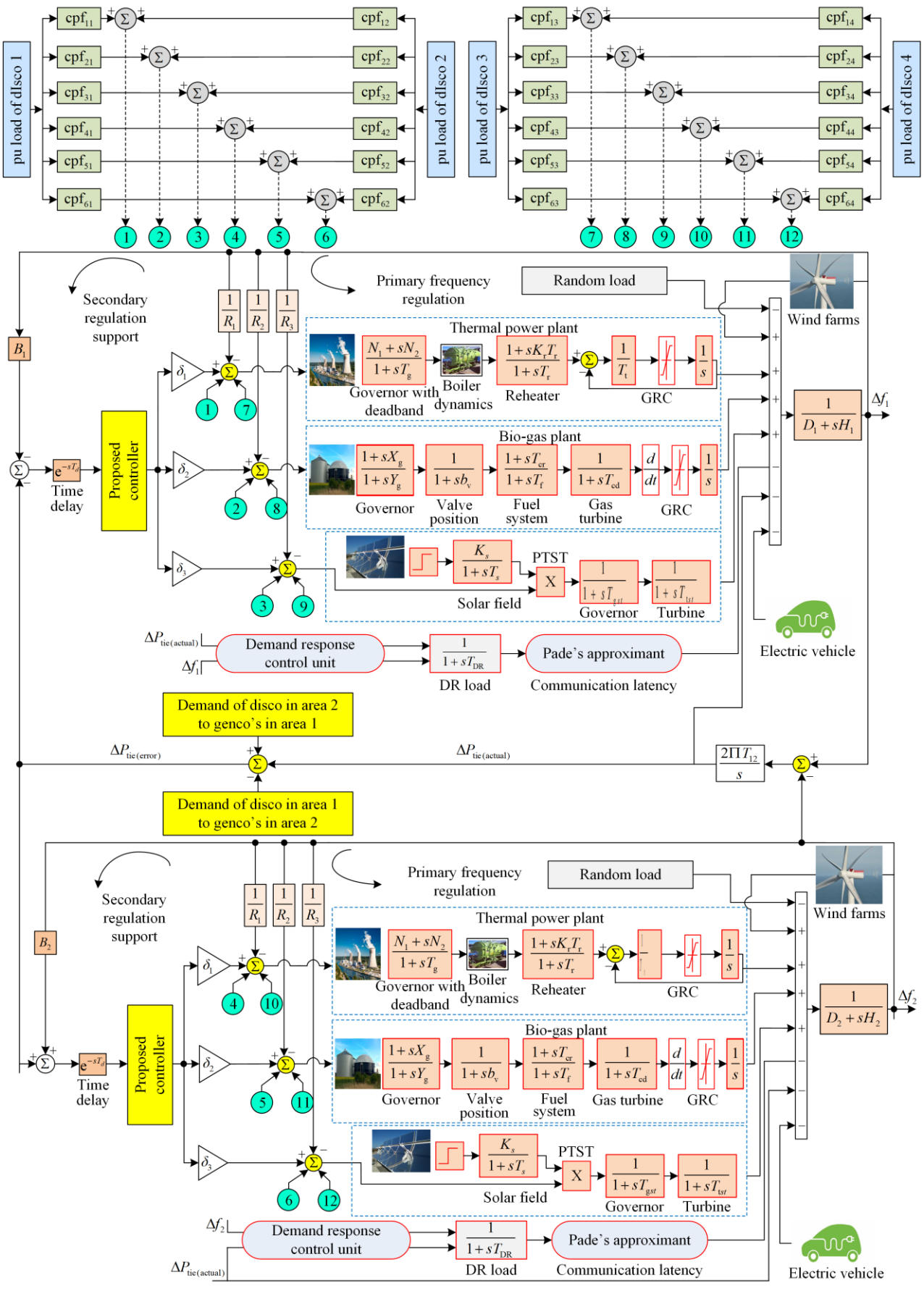

Fig. 8. Modelling of suggested deregulated hybrid power system with DR.

The communication latency is observed in [33], modelled with a 5th order Pade approximation, in [34]. As an order higher than ten may cause clustering of poles, based on [33], [34], the 5th order Pade approximation is chosen. Stability analysis is also performed by considering communication latency, which shows no negative impact on the system. The secondary controller and the system characteristics are also significant in finding a suitable order for the delay approximation. Therefore the lag in communication using Pade's approximation [34] for 5th order can be expressed as:

$$G_k(s) = \frac{-T_d^5 s^5 + 30T_d^4 s^4 - 420T_d^3 s^3 + 3360T_d^2 - 15120T_d + 30240}{T_d^5 s^5 + 30T_d^4 s^4 + 420T_d^3 s^3 + 3360T_d^2 + 15120T_d + 30240} \tag{14}$$

From (12), there is:

$$\Delta f_k(s) = \frac{\left\{\begin{matrix} H_{\Theta,k}(s)\Delta P_{\Theta,k}(s) - \Delta P_{d,k}(s) + G_k(s)\Delta P_{\mathrm{DR},k}(s) \pm \\ \Delta P_{\mathrm{EV}}(s) - \dfrac{2\pi}{s} T_{12}[\Delta f_k(s) - \Delta f_l(s)] \end{matrix}\right\}}{2H_k s + D_k + (H_{\Theta,k}(s)/R_k)} \tag{15}$$

For step change in demand, it is:

$$\Delta P_{d,k}(s) = \frac{\Delta P_{d,k}}{s} \tag{16}$$

From (12), the following expression for frequency deviation can be evaluated [33]:

$$\Delta f_k(s) = \frac{1}{\xi(s)} \left[\begin{matrix} H_{\Theta,k}(s)\Delta P_{\Theta,k}(s) - \dfrac{\Delta P_{d,k}}{s} + G_k(s)\Delta P_{\mathrm{DR},k}(s) \\ \pm\Delta P_{\mathrm{EV}}(s) - \Delta P_{\mathrm{tie},kl}(s) \end{matrix}\right] \tag{17}$$

where

$$\xi(s) = 2H_k s + D_k + \frac{H_\Theta(s)}{R_k} \tag{18}$$

The set point response of the system frequency stabilization using the final value theorem is stated as:

$$\Delta f_{(sse)} = \lim_{s\to 0} s\Delta f_k(s) = \frac{\Delta P_{\Theta,k(sse)} + \Delta P_{DR,k(sse)} - \Delta P_{d,k} \pm \Delta P_{\mathrm{EV}(sse)} - \Delta P_{\mathrm{tie},kl(sse)}}{\xi(0)} \tag{19}$$

where $\Delta P_{\Theta,k(ss)} = \lim_{s\to 0} sH_{\Theta,k}(s).\Delta P_{\Theta,k}(s)$

$$\Delta P_{\mathrm{DR},k(ss)} = \lim_{s\to 0} sG_k(s).\Delta P_{\mathrm{DR},k}(s)$$

$$\xi(0) = D_k + \frac{H_\Theta(0)}{R_k} = D_k + \frac{1}{R_k} = B \tag{20}$$

Frequency alteration at a steady point can be given as:

$$\Delta f_{(sse)} = \lim_{s\to 0} s\Delta f_k(s) = \frac{\Delta P_{\Theta,k(sse)} + \Delta P_{\mathrm{DR},k(sse)} - \Delta P_{d,k} - \Delta P_{\mathrm{tie},kl(sse)} \pm \Delta P_{\mathrm{EV}(sse)}}{D_k + \dfrac{1}{R_k}} \tag{21}$$

The stable-state error for grid stabilization phenomena of the *k*th test region will never nullify till DR regulatory loop, SR, EV, and tie-line participation exist, as shown in (21). However, DR provides further support to strengthen FR operations. If power from an adjacent area is not needed, i.e., $P_{\mathrm{tie12}} = 0$, no intervention from the EV, i.e., $P_{\mathrm{EV}} = 0$, and zero DR assistance at a steady point, then the steady-state error would remain nil. That reflects that the SR will provide the required supervision to keep supply and consumption in balance. Furthermore, the presence of DR in FR enhances the credibility of FR functioning [33]. As a result, the SR and DR control attempts (Ω) can be stated as:

$$\Delta P_{\varepsilon,k(sse)} = \delta\,\Omega \tag{22}$$

$$\Delta P_{\mathrm{DR},k(sse)} = (1-\delta)\,\Omega \tag{23}$$

where the value of regulatory participation (δ) ranges from 0 to 1 and reflects the cooperation of traditional regulatory operation. If $\delta = 1$, the DR contribution is zero, and the appropriate endeavor is performed solely by SR. Similarly, if $\delta = 0$, the DR control loop is responsible for all regulation.

V. Proposed Optimal Control and Optimization Algorithm

A. Proposed Feedback Based Modified Fuzzy (TDOF) Controller

The feedback control method is mainly used to rapidly reject disturbances before they spread to different plant sections. The effects of the feedback controller exhibit promising properties, even in cases where the plant contains nonlinearities. Fractional-order controllers (FOC) are now undergoing research and development because of their durability and superior optimal tuning than integral controllers. A tilt control methodology is a FOC extension. PID is a control scheme with the exception that the K_p measuring component is substituted with $K_{tt}s^{-1/\Phi}$ where $\Phi(\neq 0)$ is a tilt coefficient and ($K_p = K_{tt}$). The computation of fractional-order (FO) control has been deployed to test a hybrid power system to enhance dynamic performance. Differential equations are addressed by fractional calculus in non-integer controllers. Therefore, the fractional integral differential operator can be expressed as:

$$D_f = \left\{\begin{matrix} \dfrac{\mathrm{d}}{\mathrm{d}t^\sigma} & \sigma > 0 \\ 1 & \sigma = 0 \\ \displaystyle\int_0^t (\mathrm{d}\Gamma)^{-\sigma} & \sigma < 0 \end{matrix}\right\} \tag{24}$$

This study makes use of one of Oustaloup's perceived approximations. The Oustaloup filter demonstrates efficacy in handling the fractional components σ within a specific frequency range (10^{-3}, 10^3) and order 5. In order to enhance the transient stability of the system, an intelligent fuzzy logic rule-based control strategy is integrated with the designed TDOF controller. The area

control error (ACE) and its derivative are used as inputs to the fuzzy TDOF controller. The fuzzy logic rule scheme consists of three primary functions: fuzzification, decision-making, and defuzzification. Fuzzification involves the conversion of crisp input data into fuzzy data using triangular membership functions, which are employed for error, derivative of error, and output in the FLC, and five fuzzy linguistic variables as negative large (NLG), negative small (NSL), zero (ZE), positive small (PSL), positive large (PLG). The Mamdani interface mechanism is used for the fuzzy operation to make judgment calls on a rule-based approach. The centroid approach is used to do this, and is referred to as defuzzification. The TDOF controller receives the FLC's crisp output. The membership function, a crucial component of the fuzzy logic system, is visually represented in Fig. 9, which depicts how the linguistic variables are related to their respective degrees of membership. The rule base, on the other hand, governs the decision-making process within the fuzzy logic system, and is presented in Table I. It outlines the specific rules that are applied to different combinations of linguistic variables to arrive at appropriate outputs or actions. Together, the membership function and rule base play a vital role in determining the behavior and functionality of the fuzzy logic system, enabling it to handle complex and uncertain inputs and produce meaningful and accurate outputs. The capacity to tune the coefficients, as well as its accuracy and more excellent disturbance rejection capabilities, are all advantages of the recommended fuzzy logic rule-based control methodology. Some restrictions may include slightly longer optimization run time and more control parameters. The transfer function input and output relation of the modified TDOF control approach need to be calculated for FR analysis. In the specified control arrangement, $U_1(s)$ represents the output of the two-degree-of-freedom fractional-order proportional-integral (TDOF-FOPI) controller, and its transfer function can be determined as:

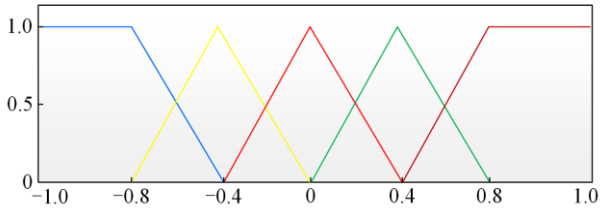

Fig. 9. Membership function structure.

TABLE I
RULE BASE FOR THE SUGGESTED ENHANCED FUZZY AUGMENTED (TDOF) CONTROLLER

ACE	ΔACE				
	NLG	NSL	ZE	PSL	PLG
NLG	NLG	NLG	NSL	NSL	ZE
NSL	NLG	NSL	NSL	ZE	PSL
ZE	NSL	NSL	ZE	PSL	PSL
PSL	NSL	ZE	PSL	PSL	PLG
PLG	ZE	PSL	PSL	PLG	PLG

$$U_1(s)=\left\{a_pQ(s)-Y(s)\right\}K_p+\left\{Q(s)-Y(s)\right\}\frac{K_i}{s^\sigma} \quad (25)$$

where a_p denotes the weight assigned to the proportional gain (K_p) for the set point; while K_i represents the coefficient for the integral gain, Q(s) and Y(s) refer to the output signals of fuzzy logic and area frequency deviation, respectively. Further simplifying (25) in terms of two input control signals, Q(s) and Y(s) yields:

$$U_1(s)=Q(s)\left(a_pK_P+\frac{K_i}{s^\sigma}\right)-Y(s)\left(K_P+\frac{K_i}{s^\sigma}\right) \quad (26)$$

By separating the proportional and integral coefficients, equation (26) can be expressed as:

$$U_1(s)=\left\{\frac{Q(s)\left(a_pK_ps^\sigma+K_i\right)}{\left(K_Ps^\sigma+K_i\right)}-Y(s)\right\}\left(K_p+\frac{K_i}{s^\sigma}\right) \quad (27)$$

The transfer function that characterizes the output of the feedback tilt derivative (TD) controller can be described as:

$$U_2(s)=K_{tt}\left(\frac{1}{s^{1/\Phi}}\right)+K_{td}\left(\frac{sN_f}{s+N_f}\right) \quad (28)$$

where K_{tt} and K_{td} denote the tilt and derivative gain coefficients; Φ represents the tilt parameter; while N_f refers to the filter derivative. The overall transfer function of the designed controller, representing the input to the plant, can be derived by evaluating (27) and (28) as:

$$U(s)=Q(s)\left[a_pK_P+\frac{K_i}{s^\sigma}\right]-Y(s)\left[K_p+\frac{K_i}{s^\sigma}\right]-Y(s)\left[\frac{K_{tt}}{s^{1/\Phi}}+\frac{K_{td}sN_f}{s+N_f}\right] \quad (29)$$

The structure of the suggested feedback control scheme-based modified fuzzy (TDOF) controller is demonstrated in Fig. 10.

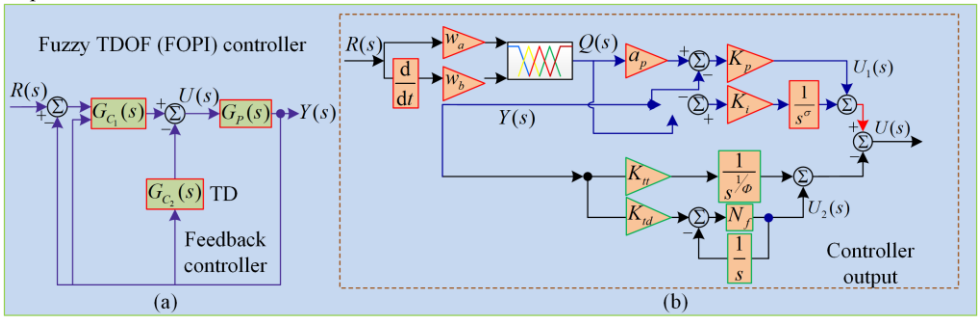

Fig. 10. Structures of controllers. (a) Proposed feedback-based controller. (b) Modified fuzzy (TDOF) controller.

B. Proposed Optimization Technique

The HHO algorithm is developed by leveraging the remarkable qualities of Harris hawks, known for their exceptional hunting abilities. These birds possess an instinctual behavior where they pursue, surround, approach, and ultimately capture their prey, such as a rabbit, through random movements. The chase is well-coordinated by the team, with one member leading the strategy to disorient the prey. In the exploration phase, the hawks visit various locations randomly to locate their target. Once located, they swiftly take advantage of the Prey's position, referred to as the moment of exploitation, and employ various tactics to capture it. HHO has been found to be helpful in various situations [31], though it has a mediocre exploitation capacity and gradually intersects at the best spot. Similar to any other optimization methods, there is the possibility of local optima entrapment, which causes a delay in converging. Further research has shown that the QOBL [30] solution has a stunning influence on global optima, unlike random and opposing solutions. By merging HHO and the QOBL paradigm, a revolutionary quasi-oppositional harris hawks optimization (QOHHO) is created to increase the HHO functionality. The proposed strategy has the following advantages over other metaheuristic optimization techniques:

1) The QOHHO method enhances population diversity, allowing for a speedier arrival of the best solution.

2) It speeds up the convergence characteristics while lowering the computational rate.

3) QOHHO is adaptive and simple to use, and can accurately extract the optimum optimal settings.

The following describes the strategy used for enhancing the HHO algorithm, where $(j=1,2,\cdots,D)$, N denotes the size of the population, and D represents the dimension of the problem. The opposite population is calculated as [30]:

$$X_{ij}^{\text{opop}} = LB_j + UB_j - X_{ij}^{\text{pop}} \tag{30}$$

where LB_j depicts a lower boundary and UB_j denotes the upper limit of controller coefficients. The quasi-opposite population is determined as [41]:

$$X_{ij}^{\text{qpop}} = \text{rand}\left(\frac{LB_j + UB_j}{2}, X_{ij}^{\text{opop}}\right) \tag{31}$$

The appropriate fittest values of X_{ij}^{opop} and X_{ij}^{qpop} are determined and the best population from the ones that have already been computed as a starting point is then taken.

Probability of quasi-opposing jumps: The quasi-opposite population [41] for the specified individuals is computed from (31) using the jumping possibility (jumping rate). The jump rate simplifies the transition from one iteration to the next with a solution that is relatively close to the previous one. N superior populations are selected from the current and quasi-opposite populations as fundamental populations for the subsequent stage. When obtaining a quasi-opposite population, the opposite and central variability values determine the lower and upper boundaries. The prey's fundamental energy and leaping power are updated as:

$$E_0 = 2\text{rand}(\,) - 1 \tag{32}$$

$$J = 2(1 - \text{rand}(\,)) \tag{33}$$

The energy of the fleeing prey is upgraded as needed, as:

$$E = 2E_0\left(1 - \frac{t}{T}\right) \tag{34}$$

On the other hand, the value of E would carry out the stages of investigation, extraction, soft besiege, and harsh besiege. If $|E| \geqslant 1$ that shows the exploration level, further updating the hawk's position as:

$$X(t+1) = \begin{cases} X_{\text{rand}}(t) - r_1\left|X_{\text{rand}}(t) - 2r_2X(t)\right|, \\ q \geqslant 0.5 \\ (X_{\text{rabbit}}(t) - X_m(t)) - r_3(LB + r_4(UB - LB)), \\ q \leqslant 0.5 \end{cases} \tag{35}$$

where $X_{\text{rabbit}}(t)$ shows the rabbit/Prey's site; $X(t)$ reflects the present status of the hawks; $X_{\text{rand}}(t)$ is the randomly chosen hawk; $X_m(t)$ describes the average position of hawks in the typical community; $|E| < 1$ specifies the stage of exploitation; $r \geqslant 0.5$ interprets the soft besiege stage; and the state vector is modified as:

$$X(t+1) = \Delta X(t) - E\left|JX_{\text{rabbit}}(t) - X(t)\right| \tag{36}$$

where $\Delta X(t)$ is the difference between the rabbit's state vector and the current stage; $|E| < 0.5$ and $r \geqslant 0.5$ denote the stage of hard besiege. Alter the status of hawks yet again, as:

$$X(t+1) = X_{\text{rabbit}}(t) - E\left|\Delta X(t)\right| \tag{37}$$

Therefore, the further step of hawks can be described by:

$$Y = X_{\text{rabbit}}(t) - E\left|X_{\text{rabbit}}(t) - X(t)\right| \tag{38}$$

As a result, if their following modification fails to meet their expectations, they will consciously take the rapid leap of:

$$Z = Y + S + LF(D) \tag{39}$$

where S denotes the arbitrary vector ($1 \times$ D); and LF exemplifies the Levy flight function; $|E| \geqslant 0.5$ and $r < 0.5$ illustrate the soft besiege with a hasty plunge, again upgrading the current state as:

$$X(t+1) = \begin{cases} Y & \text{if } F(y) < F(X(t)) \\ Z & \text{if } F(Z) < F(X(t)) \end{cases} \tag{40}$$

In this context, $|E| < 0.5$ and $r < 0.5$ represent hard besiege with a hasty plunge. Ultimately, the state of hawks can possibly be revamped from (40). Replacing $Y = X_{\text{rabbit}}(t) - E\left|X_{\text{rabbit}}(t) - X_m(t)\right|$ in (38), $X_m(t)$ corresponds to the average state of hawks as:

$$X_m(t) = \frac{1}{N}\sum_{i=1}^{N} X_i(t) \tag{41}$$

whereas N represents a state of individual hawks and $X_i(t)$ symbolizes the entire hawks. Continue the procedure until the initialized number of iterations is attained. The suggested optimization approach is also tested on a set of common standard benchmark functions [31] with a dimension of 30 and a defined number of iterations of 100.

To evaluate the effectiveness of the proposed QOHHO, a comparison is made between its figure of demerit (FOD) and that of various other optimization techniques, including recent methods of HHO, SSA, WOA, GWO, ALO, PSO, and TLBO. The FOD is a metric that quantifies the performance and convergence behaviour of the algorithms. As depicted in Fig. 11, the comparison clearly demonstrates the superiority of the suggested QOHHO algorithm. The graph cases show the convergence behaviour of the different algorithms, with the QOHHO outperforming the others in terms of achieving the desired solutions and optimizing the objective function. This result underscores the effectiveness and efficiency of the QOHHO algorithm in tackling complex optimization problems, making it a promising and competitive approach for various real-world applications. The flowchart of the suggested algorithm is shown in Fig. 12, and below is the pseudo code for the proposed algorithm.

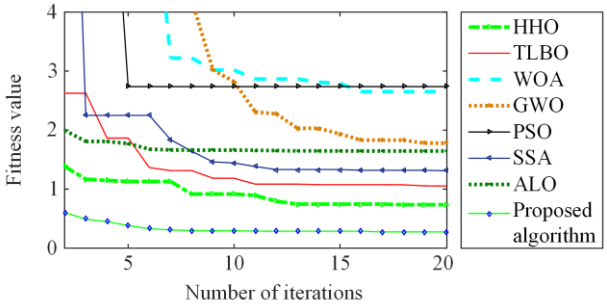

Fig. 11. Convergence plot of HHO, TLBO, WOA, GWO, PSO, SSA, ALO, and proposed algorithm.

Pseudo-code of proposed QHHO algorithm

Initialize the population $X_{ij}^{\text{pop}}(i=1,2,\cdots,N)$; $(j=1,2,\cdots,D)$ and max iterations.

Calculate the opposite population $X_{ij}^{\text{opop}} = LB_j + UB_j - X_{ij}^{\text{pop}}$.

Next, the quasi-opposite population is computed as follows:

$$X_{ij}^{\text{qpop}} = \text{rand}\left(\frac{LB_j + UB_j}{2}, X_{ij}^{\text{opop}}\right)$$

Calculate the fitness of X_{ij}^{opop} and X_{ij}^{qpop} and choose the best population from X_{ij}^{opop} and X_{ij}^{qpop}

The site of the prey and its objective function value

while (stopping criteria is not met) **do**

Determine the objective function value of hawks

Set M_{prev} as the site of prey (best site)

for (each hawk (M_i)) **do**

Renovate the initial energy E_o and jump strength J as $E_o = 2$ rand (0,1)-1, $J = 2$ (1-rand(0,1))

Renovate the E using (3)

If $|E| \geq 1$ **then** #Exploration stage

Renovate the site vector using (1)

end

If $|E| \leq 1$ **then** #Exploration stage

If $|E| \geq 0.5$ and $r \geq 0.5$ **then** #Phase -1: Soft besiege

Renovate the site vector using (5)

else if $|E| \leq 0.5$ and $r \geq 0.5$ **then** #Phase-2: Hard besiege

Renovate the site vector using (8)

else if $|E| \geq 0.5$ and $r < 0.5$ **then** # Phase-3: Soft besiege with progressive rapid dives.

Renovate the site vector using (9)

else if $|E| \leq 0.5$ and $r < 0.5$ **then** #Phase-4: Hard besiege with progressive rapid dives

Renovate the site vector using (12)

end

end

end

Return M_{prev}

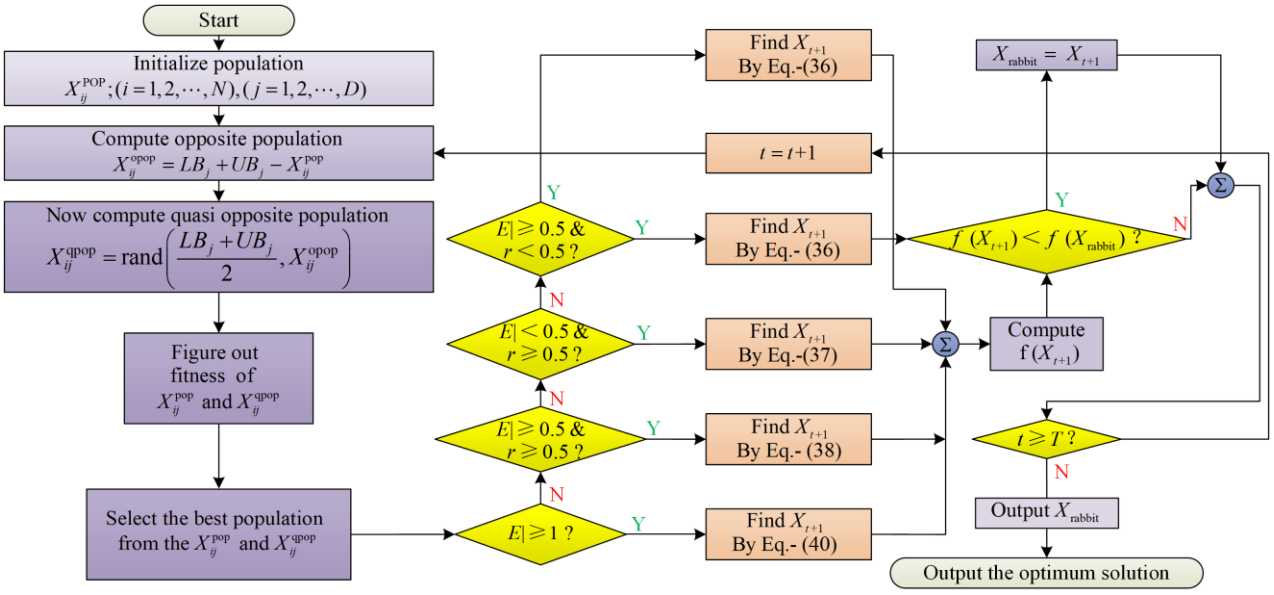

Fig. 12. Flowchart of the proposed QOHHO algorithm.

C. Stability Assessment

Stability of the feedback control system, according to classical control theories [33], is essential for reliable operation. Linear analysis is used to construct the Bode graph, which is then used to analyze the stability of the model presented in Fig. 8. The proposed approach incorporates DR support in a bilateral scenario. As seen in Fig. 13, despite the system's nonlinearities, the method exhibits relative stability. Moreover, the inclusion of DR control demonstrates that communication lag does not have an adverse effect on overall stability. This highlights the significance and effectiveness of DR support in enhancing power system stability. The frequency at which the magnitude plot intersects with the 0-dB line is called the gain crossover frequency. The phase margin (PM) is determined at this frequency. The 0-dB line is not intersected in the analyzed Bode plot, and hence the PM is infinite. The phase crossover frequency is 29.4 rad/s without DR and 90.9 rad/s with DR. In addition, incorporating DR improves the gain and phase margins (which are infinite in this case) of the analyzed model, indicating a significantly more stable system.

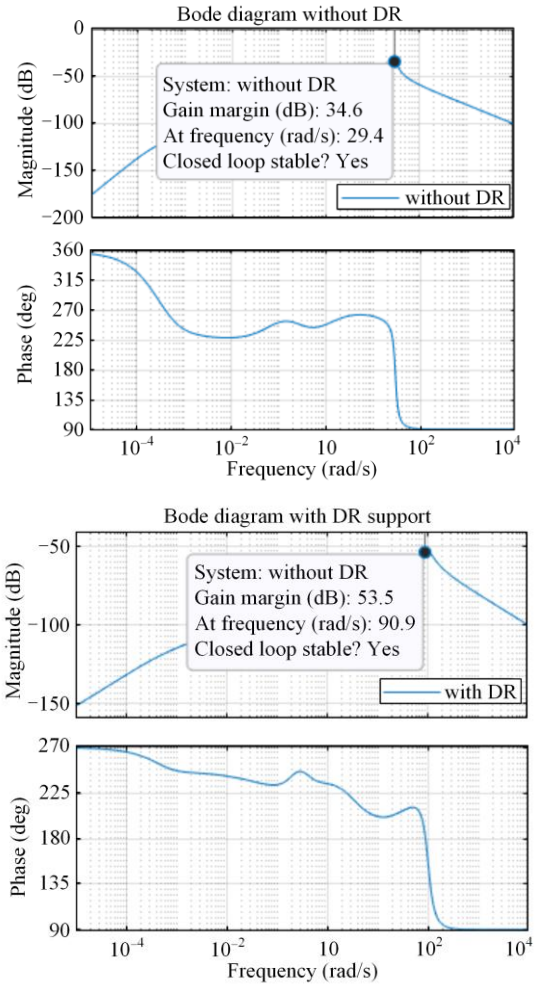

Fig. 13. Bode plot of the assessed system before and after DR regulation support for bilateral scenario.

VI. Formulation of Objective Function

The selection of appropriate objective functions is essential to any optimization process. Typical functions used in frequency stabilization are integration of squared error (ISE), integration of time squared error (ITSE), integration of absolute error (IAE), and integration of time absolute error (ITAE) [18]. Various employed objective functions by designed control algorithm are expressed below, where T is the simulation time.

The objective function ISE can be given as:

$$J_{\mathrm{ISE}} = \int_0^T (\Delta f_1^2 + \Delta f_2^2 + \Delta P_{\mathrm{tie12,error}}^2)\mathrm{d}t \tag{42}$$

where Δf_1, Δf_2 and $\Delta P_{\mathrm{tie12,error}}$ represent deviation in test area frequencies and tie-line power error alteration within the area respectively. The objective function, initially formulated as ISE with consideration of time, can be transformed into ITSE as:

$$J_{\mathrm{ITSE}} = \int_0^T (t\times\Delta f_1^2 + t\times\Delta f_2^2 + t\times\Delta P_{\mathrm{tie12,error}}^2)\mathrm{d}t \tag{43}$$

By replacing the square value of error in (42) with the absolute value of error, the ISE becomes IAE as:

$$J_{\mathrm{IAE}} = \int_0^T \left|\Delta f_1 + \Delta f_2 + \Delta P_{\mathrm{tie12,error}}\right|\mathrm{d}t \tag{44}$$

Furthermore, if the IAE is multiplied by time, as depicted in equation (43), it results in ITAE, expressed as:

$$J_{\mathrm{ITAE}} = \int_0^T (t\times|\Delta f_1| + t\times|\Delta f_2| + t\times|\Delta P_{\mathrm{tie12,error}}|)\mathrm{d}t \tag{45}$$

All four objective functions mentioned above are employed in the investigated system to acquire an appropriate objective function. However, compared with other indices, ITAE outperforms and offers comparatively better dynamic responses, and therefore, ITAE is considered then objective function for the assessed power system. Numerical values of peak overshoot (MOS) and undershoot (MUS) for frequency and tie-line power flow alteration with distinct objective functions considering bilateral scenarios are displayed in Table II.

TABLE II
DYNAMIC RESPONSE THROUGH DISTINCT PERFORMANCE INDEX FOR SCENARIO-I

Objective function	Δf_1 (Hz)	Δf_2 (Hz)	$\Delta P_{\mathrm{tie12,error}}$ (p.u.)
	MUS ($\times10^{-5}$)	MUS ($\times10^{-4}$)	MOS ($\times10^{-5}$)
ISE	−5.11	−2.91	9.18
ITSE	−4.69	−2.16	9.00
IAE	−5.02	−2.55	10.16
ITAE	**−4.13**	**−1.96**	**8.16**

VII. Deregulated Scenario

In a deregulated market, Disco of any specific region can handle Genco's available power within the test

region (unilateral agreement) or other areas (bilateral agreement). A genco–disco contract alliance can be is envisioned through a disco participation matrix (DPM) shown in (46). Entities of DPM are termed contract participation factor (CPF). The *ij*th element of DPM exhibits a fraction of the demand contracted by Disco_j from Genco_i. In this study, a system operating under a deregulated scenario consisting of three generation companies (Gencos) and two distribution companies (Discos) in each region is investigated. The system being analyzed is a deregulated two-area system, and its representation is shown in Fig. 14.

$$\boldsymbol{DPM} = \begin{bmatrix} \text{cpf}_{11} & \cdots & \text{cpf}_{14} \\ \vdots & & \vdots \\ \text{cpf}_{61} & \cdots & \text{cpf}_{64} \end{bmatrix} \tag{46}$$

In the ***DPM*** matrix, column entities' total sum could be unity. i.e.:

$$\sum_{i=1}^{NG} \text{cpf}_{ij} = 1; \text{ for } j = 1, 2, \cdots, ND \tag{47}$$

Here *N*G and *N*D exemplify the total number of Gencos and Discos, respectively. Mathematically the contracted demand of the *i*th Genco with Discos can be ensured as:

$$\Delta P_{gci} = \sum_{j=1}^{ND} \text{cpf}_{ij} \Delta P_{Lj}; \text{ for } i = 1, 2, \cdots, NG \tag{48}$$

Where ΔP_{gci} is the contracted demand of the *i*th Genco and ΔP_{Lj} is the net demand of the *j*th Disco. The scheduled tie-line power is endowed as:

$$\Delta P_{\text{tie12,scheduled}} = [\text{Demand of Discos existing in the second area from the first area Gencos}] - [\text{Demand of Discos existing in the first area from the second area Gencos}] \tag{49}$$

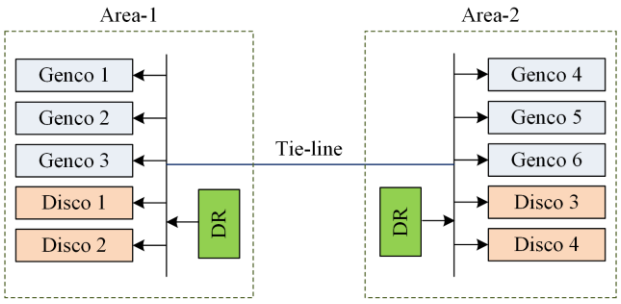

Fig. 14. Two areas deregulated investigated system.

The expression for the tie-line power error can be expressed by:

$$\Delta P_{\text{tie12,error}} = \Delta P_{\text{tie12,actual}} - \Delta P_{\text{tie12,scheduled}} \tag{50}$$

The tie-line power error decreases when the actual tie-line power approaches the scheduled power limit at equilibrium.

The relative area control error (ACE) signal for both area-1 and area-2 is generated by considering the tie-line power error, frequency biasing factor (B), and regional frequency deviation. The expressions for ACE in area-1 (ACE1) and area-2 (ACE2) can be illustrated as:

$$\text{ACE}_1 = B_1 \Delta f_1 + \Delta P_{\text{tie12,error}} \tag{51}$$

$$\text{ACE}_2 = B_2 \Delta f_2 + a_{12} \Delta P_{\text{tie12,error}} \tag{52}$$

where $a_{12} = -\frac{P_{cr1}}{P_{cr2}}$; while P_{cr1} and P_{cr2} are the rated capacity of the first and second areas respectively.

VIII. Results and Discussion

In this study, the response of the investigated system to a 1% step disturbance under a deregulated scenario is analyzed using the FR scheme with DR. The system comprises three Gencos (thermal, biogas, and PTST) and two Discos in each test area. A GRC of 3% per minute (i.e., 0.0005/s), GDB ($\text{N1} = 0.8, \text{N2} = -0.2/\text{Pi}$), and BD are adopted for the thermal power plant, while a GRC of 20% per minute is considered for the biogas plant. A communication lag of 0.1 s is considered the nonlinearity in the system. Each examined area can produce up to 2000 MW with a frequency of 50 Hz, and the optimum power transfer proficiency of the tie-line is assumed to be 200 MW. Since both areas are identical, the ACE participation factors (APF) for thermal, biogas, PTST, and EV in each area are assumed to be 0.4, 0.3, 0.2, and 0.1, respectively. The ratings of various components of the test two-area power system are included in the Appendix A. Investigations carried out considering bilateral transactions for distinct scenarios are illustrated below.

A. Scenario-I: Bilateral Transaction

For bilateral transactions, the Discos can enter into a power agreement with the Gencos of any test areas. This agreement is described in (53), where each Disco requires a step load of 0.005 p.u..

$$\boldsymbol{DMP} = \begin{array}{c} \\ \text{G}_1 \\ \text{G}_2 \\ \text{G}_3 \\ \text{G}_4 \\ \text{G}_5 \\ \text{G}_6 \end{array} \begin{array}{c} \begin{array}{cccc} \text{D}_1 & \text{D}_2 & \text{D}_3 & \text{D}_4 \end{array} \\ \begin{bmatrix} 0.25 & 0.25 & 0.20 & 0.30 \\ 0.20 & 0.25 & 0.20 & 0.15 \\ 0.05 & 0 & 0.10 & 0.05 \\ 0.20 & 0.30 & 0.30 & 0.25 \\ 0.20 & 0.20 & 0.10 & 0.15 \\ 0.10 & 0 & 0.10 & 0.10 \end{bmatrix} \end{array} \tag{53}$$

where G_1, G_2, G_3 are Gencos of area-1; similarly G_4, G_5, G_6 are Gencos of area-2; D_1, D_2 are Discos of area-1; and D_3, D_4 are Discos of area-2.

In this study, two strategies are examined for system response: one without DR, denoted as strategy 1, and

the other incorporating DR, denoted as strategy 2. The corresponding responses for both strategies are depicted in Fig. 15, allowing for a visual comparison of their dynamic behaviours. The analysis clearly demonstrates that integrating DR leads to notable system performance enhancements. The inclusion of DR not only contributes to improved system stability but also provides valuable support for frequency regulation services. These findings reflect the significance and effectiveness of DR as a crucial tool in power system operation and control, offering valuable insights for future research and practical implementation. Furthermore, to quantitatively demonstrate the benefits of DR, a bar chart is presented in Fig. 16, which highlights the improvement in system dynamics achieved by implementing DR as compared to the response without DR. QOHHO Optimized designed controller coefficients for Scenario-I are reported in Table III and the improvement in the dynamic response of the test power system considering DR strategy is presented in Table IV. At steady state, the scheduled tie line power can be computed as [12]:

$$\begin{cases} \Delta P_{\text{tie12,scheduled}} = (\text{Demand of Discos in area-2 from Gencos in area-1}) - (\text{Demand of Discos in area-1 from Gencos in area-2}) \\ \Delta P_{\text{tie12,scheduled}} = \sum_{i=1}^{3}\sum_{j=3}^{4} \text{cpf}_{ij}\Delta PL_j - \sum_{i=4}^{6}\sum_{j=1}^{2} \text{cpf}_{ij}\Delta PL_j \end{cases} \tag{54}$$

The tie-line error is represented as the difference between the actual and scheduled tie-line power [11], and can be expressed as:

$$\Delta P_{\text{tie2, error}} = \Delta P_{\text{tie2, actual}} - \Delta P_{\text{tie2, scheduled}} \tag{55}$$

$$\begin{aligned} \Delta P_{\text{tie12,scheduled}} =& [(\text{cpf}_{13} + \text{cpf}_{14} + \text{cpf}_{23} + \text{cpf}_{24} + \\ & \text{cpf}_{33} + \text{cpf}_{34}) \times \Delta PL_j] - \\ & [(\text{cpf}_{41} + \text{cpf}_{42} + \text{cpf}_{51} + \text{cpf}_{52} + \\ & \text{cpf}_{61} + \text{cpf}_{62}) \times \Delta PL_j] = \\ & [(0.2+0.3+0.2+0.15+0.10+0.05)\times 0.005] - \\ & [(0.2+0.3+0.20+0.20+0.10+0)\times 0.005] = \\ & 0 \text{ p.u.} \end{aligned} \tag{56}$$

At steady state, both $\Delta P_{\text{tie2, error}}$ and $\Delta P_{\text{tie2,scheduled}}$ are zero. Therefore, $\Delta P_{\text{tie12, actual}}$ is also zero, i.e.:

$$\Delta P_{\text{tie12,actual}} = \Delta P_{\text{tie12,error}} + \Delta P_{\text{tie12,scheduled}} = 0 + 0 = 0 \text{ p.u.} \tag{57}$$

The theoretical value of $\Delta P_{\text{tie12,actual}}$, is calculated in (57), and its corresponding simulated response is shown in Fig. 15(d). A bilateral agreement between the Discos and Gencos is presented in (53), where individual Discos requires a step load of 0.005 p.u. The theoretical values of all GENCOs are calculated in (58)–(63), and the simulated response is depicted in Figs. 15 (e) and (f).

$$\text{G}_1 = (0.25+0.25+0.2+0.3)\times 0.005 = 5\times 10^{-3} \text{ p.u.} \tag{58}$$

$$\text{G}_2 = (0.20+0.25+0.2+0.15)\times 0.005 = 4\times 10^{-3} \text{ p.u.} \tag{59}$$

$$\text{G}_3 = (0.05+0+0.10+0.05)\times 0.005 = 1\times 10^{-3} \text{ p.u.} \tag{60}$$

$$\text{G}_4 = (0.20+0.30+0.30+0.25)\times 0.005 = 5.25\times 10^{-3} \text{ p.u.} \tag{61}$$

$$\text{G}_5 = (0.20+0.20+0.10+0.15)\times 0.005 = 3.25\times 10^{-3} \text{ p.u.} \tag{62}$$

$$\text{G}_6 = (0.10+0+0.10+0.10)\times 0.005 = 1.5\times 10^{-3} \text{ p.u.} \tag{63}$$

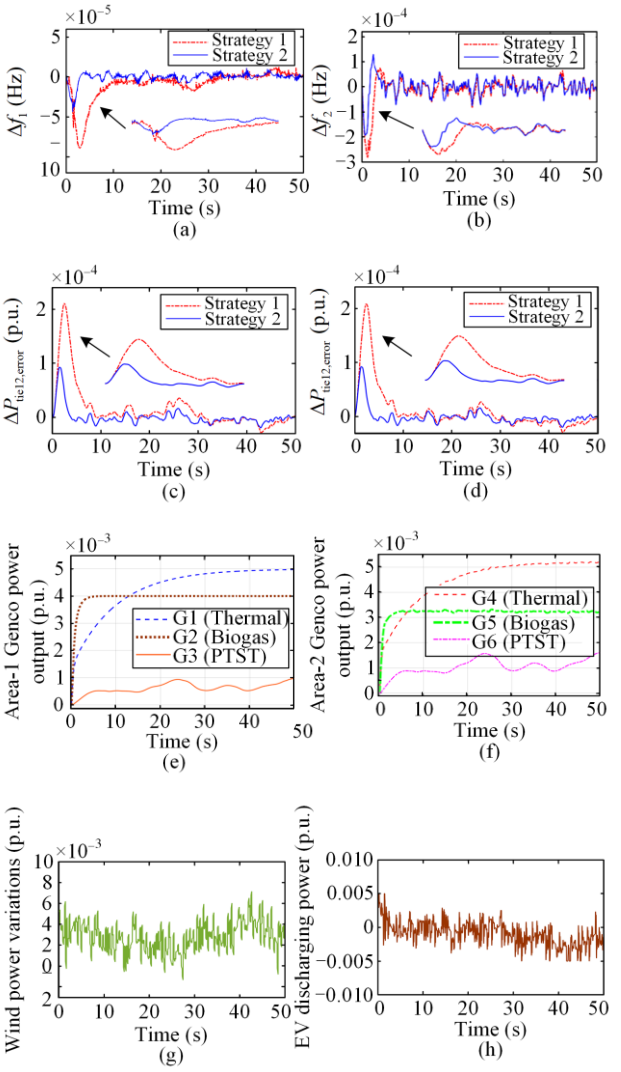

Fig. 15. Dynamics of Scenario-I. (a) Frequency change in the first area. (b) Frequency change in the second area. (c) Change in tie-line power error. (d) Change in actual tie-line power. (e) Genco's power output with DR in the first area. (f) Genco's power output with DR for the second area. (g) Wind power variation (h) Deliverance power of EV.

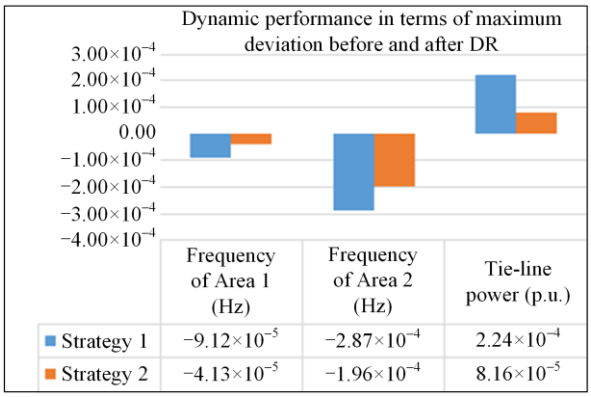

Fig. 16. A bar chart highlighting the influence of DR.

TABLE III
OPTIMIZED PARAMETERS FOR SCENARIO-I

Optimized parameters with DR		Optimized parameters without DR	
Area-1	Area-2	Area-1	Area-2
$K_{i1}=0.789$	$K_{i2}=0.781$	$K_{i1}=0.812$	$K_{i2}=0.678$
$K_{P1}=1.541$	$K_{P2}=2.180$	$K_{P1}=0.917$	$K_{P2}=1.327$
$a_{p1}=0.487$	$a_{p2}=0.470$	$a_{p1}=0.971$	$a_{p2}=0.961$
$\sigma_1=0.897$	$\sigma_2=1.120$	$\sigma_1=0.417$	$\sigma_2=0.659$
$K_{it1}=2.187$	$K_{it2}=0.977$	$K_{it1}=0.598$	$K_{it2}=2.916$
$\Phi_1=2.480$	$\Phi_2=2.950$	$\Phi_1=2.732$	$\Phi_2=2.872$
$K_{td1}=1.790$	$K_{td2}=2.189$	$K_{td1}=0.987$	$K_{td2}=1.890$
$N_{f1}=40.870$	$N_{f2}=29.317$	$N_{f1}=41.54$	$N_{f2}=60.1$
$w_{a1}=0.456$	$w_{a2}=0.767$	$w_{a1}=0.678$	$w_{a2}=0.432$
$w_{b1}=0.916$	$w_{b2}=0.812$	$w_{b1}=0.124$	$w_{b2}=0.192$
$T_{DR1}=51.7703$	$T_{DR2}=45.143$	–	–

TABLE IV
COMPARISON OF THE MAXIMUM DEVIATION IN THE TEST SYSTEM'S TRANSIENT BEHAVIOR

System response	Maximum deviation without DR	Maximum deviation with DR
Δf_1 (Hz)	-9.12×10^{-5}	-4.13×10^{-5}
Δf_2 (Hz)	-2.87×10^{-4}	-1.96×10^{-4}
$\Delta P_{tie12,error}$ (p.u.)	2.24×10^{-4}	0.81×10^{-4}

B. Scenario-II: Unraveling the Dynamic Effects of Nonlinearities

In this scenario, functional power systems, including thermal and biogas power plants, have a GRC. This constraint limits the rate at which power can be generated, preventing it from reaching excessive levels. Without the GRC, generators are vulnerable to severe transient disturbances, which are undesirable. Therefore, a comprehensive evaluation of the AGC must consider the GRC. For the system in question, the GRC rates are limited to 3% per minute for thermal units and 20% per minute for biogas units. In addition, the dead band of the thermal speed governor allows for an increase or decrease in speed for a given position of the governor control valves before a valve position changes. This can significantly impact the system's response. In the presence of a dead band and GRC, a dead-band limiting value of 0.06% is used because the system becomes highly nonlinear, even for small load changes,

Making the optimization problem quite challenging. Because of the increased complexity of interconnected restructured power systems, communication channel delay significantly affects AGC performance. Time delay (TD) can destabilize a system and harm its effectiveness. In the studies, ACE's output signal is delayed by 0.1s to account for this. Considering Scenario I, the impact of non-linearities on the dynamic response of the system is investigated. To gain a comprehensive understanding of the system's behavior in various conditions, five cases are explored, each incorporating specific non-linearities. The first case serves as a baseline for comparison involves no system non-linearities. In the second case, GDB is introduced to observe its influence on the dynamic response. The third case incorporates GDB and GRC to examine their combined effects on the system's behaviour. Building upon the third case, the fourth case includes BD, studying how its addition impacts the dynamic response. In the fifth case, it further augments the system with TD to explore the collective impact of all the considered non-linearities on system performance. The area frequencies and tie-line power responses corresponding to each evaluated case are presented in Fig. 17. In this context, through careful evaluation from Fig. 17, it can be seen that when GDB, GRC, and BD are evaluated together, the dynamic response experiences a significant drop. This suggests that these non-linearities notably affect the system behaviour. Additionally, the inclusion of significant TD further worsens the system dynamic effectiveness.

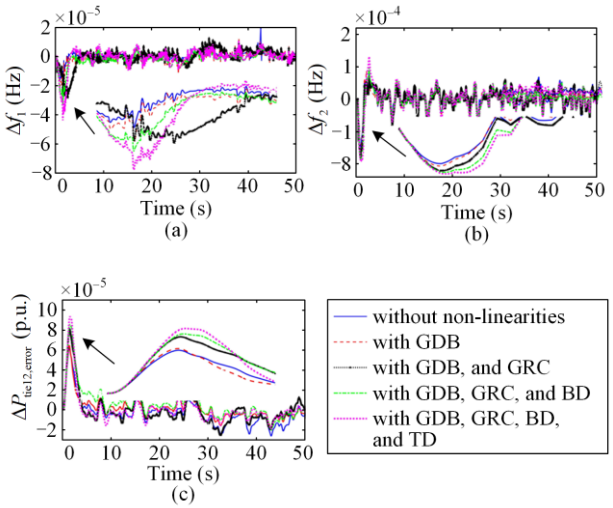

Fig. 17. System dynamic response without and with nonlinearities. (a) Frequency change in the first area. (b) Frequency change in the second area. (c) Change in tie-line power.

C. Scenario-III: Unraveling Sensitivity: A Thorough and Comprehensive Assessment

Sensitivity computation is performed on the permanence of the proposed algorithm tuned designed modified feedback control-based fuzzy TDOF controller under extensive alteration in the power grid parameters and loading. In the context of an actual power grid, accurately determining parameters like damping coefficients (D) and inertia (H) can be quite challenging. Due to this uncertainty, it is widely acknowledged that these values may deviate by approximately 25% from their rated values. As part of the sensitivity analysis, each area parameter is individually assessed with a ±25% variance to evaluate the system response in varying conditions. The outcomes of this sensitivity analysis are depicted in Fig. 18, which demonstrates the system's performance when there are significant changes in grid parameters. Despite the substantial variations in these crucial parameters, the recommended control algorithm exhibits robust characteristics, maintaining stable system dynamics. This observation highlights the reliability and feasibility of the suggested controller, demonstrating its ability to adapt to uncertainties and ensuring the effective regulation of frequency in the power grid. The results further reflect the controller's suitability for real-world applications and its potential to enhance the stability and performance of power systems in dynamic scenarios.

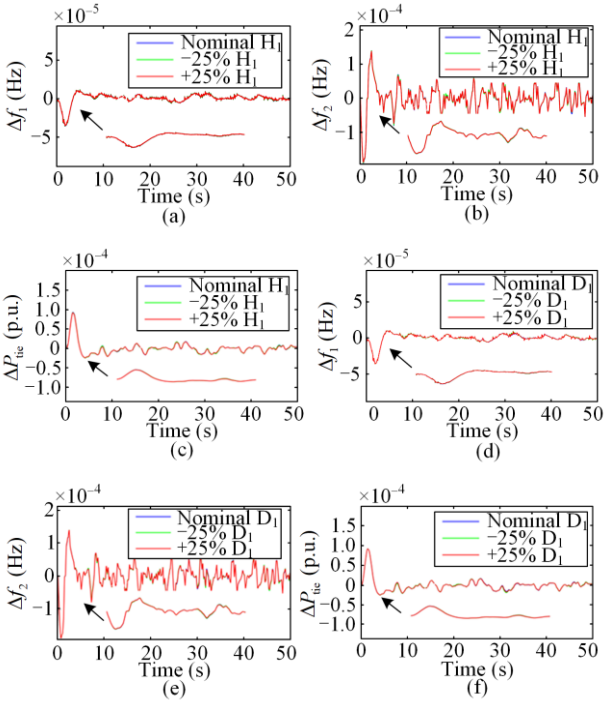

Fig. 18. (a) Frequency deviation in area-1 for ± 25% variation in H_1.(b) Frequency deviation in area-2 for ± 25% variation in H_1. (c) Deviation in tie-line power error for ± 25% variation in H_1. (d) Frequency deviation in area-1 for ± 25% variation in D_1. (e) Frequency deviation in area-2 for ± 25% variation in D_1. (f) Deviation in tie-line power for ± 25% variation in D_1.

D. Scenario-IV: Performance Comparison with other Robust Controllers

The attributes of the suggested control strategy for the system under investigation are examined and compared with those of the PIDN, TIDN, TDOF(FOPI), TDOF(FOPI)-TID, and TDOF(FOPI)-TD controllers. The computed optimized parameters for the controller coefficients in each case are displayed in Table V. In this study, the variation in the frequency of area-1 is assessed by employing the studied and designed control scheme. As depicted in Fig. 19, the system dynamic characteristics provide valuable insights into the control methodology that influences FR services. The findings indicate that the designed controller is highly effective in maintaining the frequency within the desired limits, leading to a more stable and reliable power system response in area-1. The critical observations derived from the comparison of results firmly establish the supremacy of the proposed control algorithm over various other control methodologies. Also, Fig. 20 presents a visual representation of the enhanced performance achieved through the implementation of the suggested controller than the other tested control strategies.

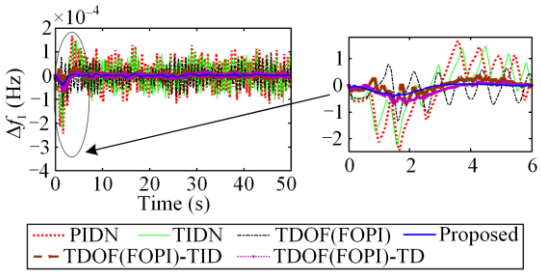

Fig. 19. Comparison of the dynamic response of PIDN, TIDN, TDOF (FOPI), TDOF (FOPI)-TID with the proposed.

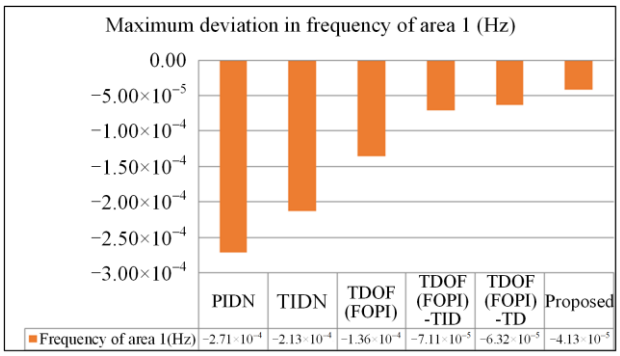

Fig. 20. Bar chart characterizing the improvement with the proposed control approach for maximum deviation in area-1 frequency.

The graph clearly illustrates a substantial reduction in frequency deviations obtained with the proposed control strategy, demonstrating its superiority over other control methods. These results emphasize the significance and potential of the designed controller in achieving improved frequency regulation and overall system efficiency in area-1. A comprehensive performance evaluation of diverse controllers, considering various

performance characteristics is presented in Table VI. In this context, the proposed controller stands out with distinct advantages compared to other control schemes. Notably, it excels in terms of its exceptional disturbance elimination capability, showcasing remarkable improvements in dynamic performance and achieving a rapid performance rate. While the proposed controller showcases considerable strengths, it is imperative to acknowledge that it also has certain limitations. A notable drawback is the augmented number of controller coefficients that necessitate careful consideration during optimization, resulting in increased computational run time. Despite these drawbacks, the proposed controller's overall performance superiority makes it a promising choice in robust control applications. Table VII highlights this notable improvement, demonstrating the reduced maximum deviation of area-1 frequency accomplished by the proposed technique.

TABLE V
QOHHO OPTIMIZED PIDN, TIDN, TDOF (FOPI), TDOF (FOPI)-TID, TDOF (FOPI)-TD AND PROPOSED CONTROLLER GAINS

Controllers		K_i	K_P	K_D	a_P	σ	K_{ti}	Φ	K_{ti}	K_{td}	N_f	w_a	w_b	T_{DR}
PIDN	A-1	0.7327	1.0208	0.9889							29.0434			
	A-2	0.7156	1.0944	0.7689							21.8793			
TIDN	A-1	1.0000	0.8245	0.5840				2.0000			32.5050			
	A-2	1.0345	1.1691	1.3863				2.0431			11.9811			
TDOF (FOPI)	A-1	0.0025	0.1750		0.0477	0.5904								
	A-2	0.0012	0.2205		0.0012	0.4273								
TDOF	A-1	1.5422	0.0751		0.2176	0.2277	0.3623	2.0000	0.1690	0.3019	31.7303			10.0098
(FOPI)-TID	A-2	0.5499	1.5013		0.8089	0.6484	2.0000	2.0000	0.2361	1.3202	32.9860			33.6677
TDOF	A-1	0.9523	1.3017		0.8072	0.7672	2.0000	3.0000		2.0000	50.0000			42.6803
(FOPI)-TD	A-2	0.9209	2.0000		1.0000	1.0000	1.0777	3.0000		1.1378	29.7574			32.8134
Proposed	A-1	0.7891	1.5418		0.4872	0.8972	2.1800	2.4800		1.7900	40.8700	0.456	0.916	51.7703
	A-2	0.7814	2.1800		0.4700	1.1200	0.9777	2.9500		2.1898	29.3174	0.767	0.812	45.1434

E. Scenario-V: Case Study

The proposed technique has been rigorously tested under dynamic conditions, where random load fluctuations and system non-linearities are considered within a bilateral scenario. Figure 21 (a), shows the varying load disturbance applied to the test system, which adds a realistic and challenging aspect to the evaluation. The corresponding variance in area-1 frequency is presented in Fig. 21 (b), providing insights into how the system responds to these fluctuations. Additionally, to demonstrate the efficacy of the proposed algorithm with the suggested controller, a thorough comparison is conducted with prior research work from [42], [43], specifically focusing on Poolco-based transactions. The outcomes of this comparison are depicted in Fig. 22, highlighting the enhanced dynamic response achieved by the proposed technique. Subsequently, the bar graph in Fig. 23 clearly illustrates the substantial improvement in the maximum deviation of system performance attained with the suggested controller, solidifying its superiority over alternative control methodologies. For a comprehensive understanding, the controller gain values and the dynamic responses are thoroughly investigated in Tables VIII and IX, respectively. The results consistently demonstrate the superiority of the proposed modified TDOF controller over the other control strategies used in the comparative study. Moreover, in consideration of recent a advancements in the field, the dynamic characteristics of the system as reported in [44] are assessed and its performance with the designed controller are evaluated. As illustrated in Fig. 24, the proposed control scheme demonstrates superior performance in terms of maximum deviation, thus confirming its effectiveness across various scenarios.

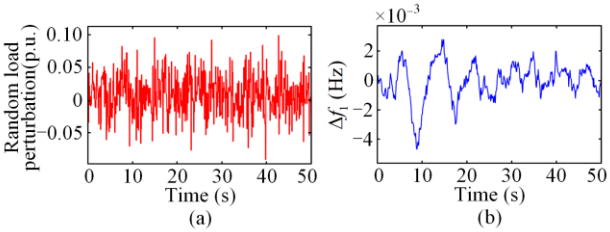

Fig. 21. Characteristic curves. (a) Random demand. (b) Frequency deviation in area-1.

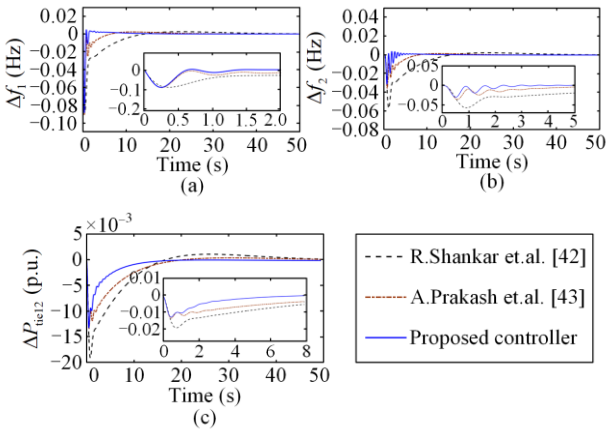

Fig. 22. Comparative dynamic response with previous work in [42], [43]. (a) Frequency change in first area. (b) Frequency change in second area. (c) Change in tie-line power error.

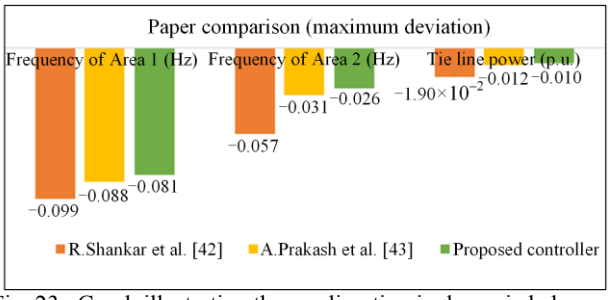

Fig. 23. Graph illustrating the amelioration in dynamic behaviour with the suggested controller against work in [42], [43].

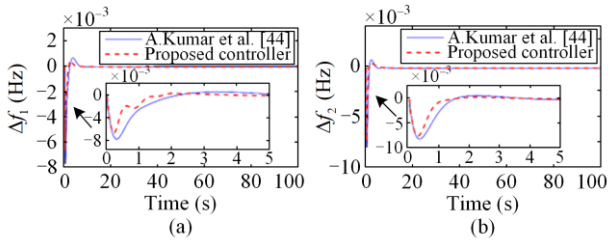

Fig. 24. Comparative dynamic response with published work [44]. (a) Frequency change in first area. (b) Frequency change in second area.

TABLE VI
ADVANTAGES AND DRAWBACKS OF THE PROPOSED CONTROL SCHEME IN CONTRAST TO OTHER EXISTING ROBUST CONTROL METHODOLOGIES

S. No.	Controllers	Performance characteristics evaluation				
		Disturbance elimination capability	Dynamic Response	Performance rate	Gain coefficients	Optimization run time
1	PIDN	Very low	Moderate	Slow	4	Less
2	TIDN	Low	Good	Average	5	Less
3	TDOF (FOPI)	Normal	Better than TIDN	Fast	4	Less
4	TDOF (FOPI)-TID	High	Better than TDOF (FOPI)	Faster than TDOF (FOPI)	9	Bit more
5	TDOF (FOPI)-TD	High	Better	Moderate	8	Bit more
6	Proposed	Excellent	Far better	Rapid	10	More

TABLE VII
COMPARISON OF THE PROPOSED CONTROLLER'S MAXIMUM DEVIATION IN AREA-1 FREQUENCY WITH OTHER EXISTING ROBUST CONTROL METHODOLOGIES

Controllers	PIDN	TIDN	TDOF(FOPI)	TDOF(FOPI)-TID	TDOF(FOPI)-TD	**Proposed**
Δf_1 (Hz)	-2.71×10^{-4}	-2.13×10^{-4}	-1.36×10^{-4}	-7.11×10^{-5}	-6.32×10^{-5}	**-4.13×10^{-5}**

TABLE VIII
OPTIMIZED PARAMETERS OF THE PROPOSED CONTROLLER FOR [42], [43]

Proposed controller	Gain									
	K_i	K_p	a_p	σ	K_{tt}	Φ	K_{td}	N_f	w_a	w_b
A-1	1.892	1.756	0.954	0.918	1.071	2.501	1.431	39.33	0.118	0.494
A-2	0.935	1.596	0.050	0.941	1.801	2.543	1.908	82.72	0.321	0.871

TABLE IX
COMPARED DYNAMIC RESPONSE FOR THE PUBLISHED WORK IN [42], [43]

	Δf_1		Δf_2		$\Delta P_{tie12,error}$	
	MUS	$T_S(s)$	MUS	$T_S(s)$	MUS	$T_S(s)$
R. Shankar et al. [42]	−0.099	40.10	−0.057	42.12	−0.019	45.19
A. Prakash et al. [43]	−0.088	9.13	−0.031	10.12	−0.012	31.33
Proposed controller	−0.081	1.77	−0.026	8.67	−0.010	27.89

The improvement chart presented in Fig. 25 demonstrates the effectiveness of the designed control algorithm compared to the previously work [44]. The improvement in the maximum deviation of [44] with the proposed controller is further presented in Table X. In conclusion, this comprehensive study illuminates the potential of the proposed technique in handling complex scenarios involving random load fluctuations and non-linearities in a bilateral context. The results consistently demonstrate the effectiveness of the suggested controller, leading to enhanced system performance and reduced frequency deviations compared to previous research work. These findings substantiate the practical applicability and relevance of the designed control algorithm in real-world power system operations.

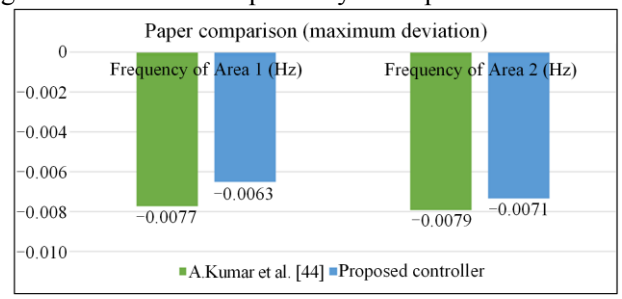

Fig. 25. In addition to recent work [44] the chart shows the improvement in maximum deviation with the suggested control algorithm.

TABLE X
COMPARED DYNAMIC RESPONSE OF [44]

System response	A. Kumar et al. [44]	Proposed
Δf_1 (Hz)	−0.0077	−0.0063
Δf_2 (Hz)	−0.0079	−0.0071

F. Scenario-VI: Experimental HIL Evaluation

In this scenario, the proposed control system's realistic execution and reliability are thoroughly evaluated using the OPAL-RT OP4510 platform. The necessity for OPAL-RT validation arises because of several key factors. First, offline simulations may lack glitches and delays that are present in real-world power systems. These discrepancies can significantly impact control system performance and may lead to misleading conclusions if not adequately considered. OPAL-RT's real-time high-fidelity models can address this issue, offering a more accurate representation of actual system behaviour. Secondly, the OPAL-RT platform enables hardware-in-the-loop (HIL) simulations, which are essential for verifying the control system's effectiveness in real-time scenarios. HIL configurations integrate physical hardware components with real-time simulation models, allowing researchers to test their control algorithms under realistic conditions. This approach helps to uncover potential issues and validates the system response. In Fig. 26, the HIL configuration is depicted, comprising crucial components for the experiments. The use of an OPAL-RT device facilitates real-time modelling, which is crucial for studying power system dynamics in a time-critical manner. The desktop acting as a host further enables seamless execution of the programming required for the real-time simulation. In addition, the incorporation of a router is vital to establish connections and facilitate smooth data exchange between the host, peripherals, and the OPAL-RT platform. This ensures accurate and reliable communication between all components, avoiding any potential disturbances in the experiment. Figure 27 presents the transient performance of the analysed system using the OPAL-RT OP4510 with DR assistance. The results obtained from these OPAL-RT simulations serve as a crucial validation step for the proposed control technique.

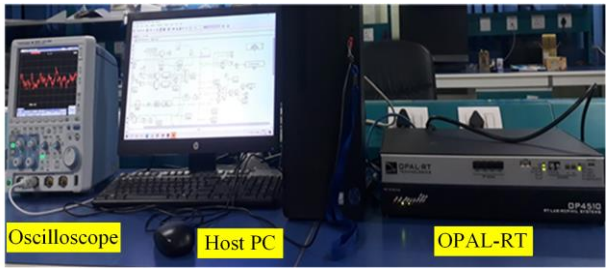

Fig. 26. Setup for real-time experiment.

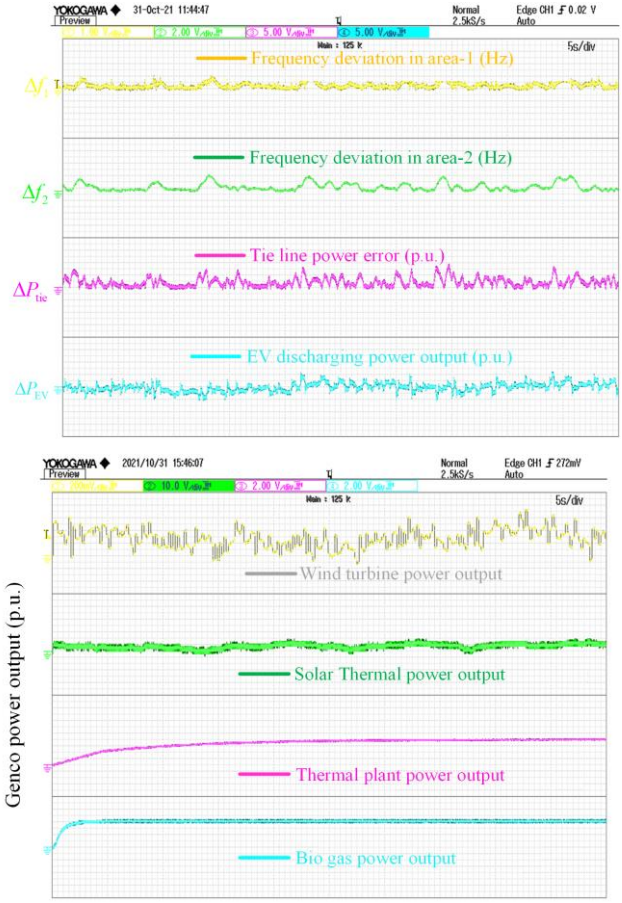

Fig. 27. Transient performance of the analyzed system. (a) The test system's HIL dynamic characteristics. (b) Power output of Genco's.

The discussions on all the aforementioned scenarios can be summarized as follows: first, the investigation focuses on the competency of the DR strategy in enhancing the dynamic characteristics of the test system, taking into account the integration of variable RES. Additionally, a comprehensive evaluation is conducted to assess the impact of system non-linearities on the dynamic performance of the system. The proposed controller's robustness is thoroughly examined by considering variations in system parameters. To assess its resilience, a comprehensive comparison is conducted between the performance of the designed controller and those of other robust controllers, namely PIDN, TIDN, TDOF (FOPI), TDOF (FOPI)-TID, and TDOF (FOPI)-TD. The effectiveness of the designed control algorithm is also tested against recently published work. Lastly, to validate the practical realization and performance of the suggested control scheme, HIL analysis using OPAL-RT OP4510 is performed. Overall, the findings of this study highlight the potential of the DR strategy in improving the dynamic response of the test system with variable RES and emphasize the robustness and practical applicability of the proposed control approach.

IX. Conclusion

This paper proposes a DR strategy for improving frequency stabilization in a deregulated power system, particularly in the presence of varying demand and intermittent behaviour of RES. To analyse the dynamic response of the test system, a QOHHO-tuned fuzzy logic control topology-based modified TDOF controller, termed a fractional order proportional integral-tilt derivative scheme, is designed. Moreover, the robustness of the designed control scheme is verified by comparing the dynamic performance with other control methodologies. To investigate the DR impact on a deregulated test system, the sensitivity of the system is evaluated, followed by an analysis for randomly varying demand. In addition, a comparison with relevant published work and a real time experimental analysis using OPAL-RT OP4510 are provided for the practical realizations of the test system.

The primary results of the analysis are:

1) Detailed examination of the analysed deregulated power network employing DR methodology significantly ameliorates frequency regulation analysis.

2) A comparative performance evaluation of the QOHHO-based developed controller and other existing resilient controllers, and its robustness to parametric changes, reveals its ascendancy. Both with and without DR participation, the stability of the test model under investigation is assessed, while the gain and phase margin increase because of the DR share, indicating increased stability and efficiency.

3) The extent of the resilience of the designed control algorithm is assessed through applying substantial fluctuations in the parameters and unpredictable load variations. The comparative examination of the system features substantiates the potency of the devised regulator compared to other examined durable control schemes and prior published works.

4) The OPAL-RT OP4510 is used to conduct a realistic estimation, which demonstrates the viability of the suggested regulation technique.

The present study explores a deregulated power system that consists of two regions. Further, in the future, the investigations can be extended to three or even four regions where research effort should prioritize the DR methodologies to tackle the frequency stabilization challenges, particularly in the light of emerging cyber threats.

Appendix A

$H_k = 10$ p.u., $D_k = 1$, , $T_{fd} = 0.2$ s, $\delta_1 = 0.4$, $\delta_2 = 0.3$, $\delta_3 = 0.2$, $\delta_4 = 0.1$, GRC of thermal = 0.0005 s, Capacity of the first (P_{cr1}) and second areas (P_{cr2}) = 2000 MW, $a_{12} = -1$, system's anticipated loading = 0.5, $T_{k1} = 0.0860$ p.u. MW/rad. $K_s = 1.8$, $T_s = 1.8$ s, $T_{gst} = 3$ s, $T_{tst} = 3$ s, $B_k = 0.4250$ p.u. MW/Hz, $R_{\text{ev}} = 2.4$ p.u. , $K_{\text{ev}} = 1$ s , $T_{\text{ev}} = 1$ s, $R_{1k} = R_{2k} = R_{3k} = 2.40$ p.u. MW/Hz, $N_{\text{ev}} = 10000$. The installed ratings of thermal, biogas, PTST, EV, and wind are 800 MW, 600 MW, 400 MW, 200 MW, and 21.80 MW, respectively.

Acknowledgement

The authors appreciate the LAB support provided by the (TLC-IOT) Laboratory at the Indian Institute of Technology, Patna (IITP) for analyzing the practicalities of the proposed control scheme.

Authors' Contributions

Abhishek Saxena: simulation and real-time validation, programming, designed controller, writing original draft. Ravi Shankar: supervision, methodology, writing review & editing.

Funding

Not applicable.

Availability of Data and Materials

Not applicable.

Declarations

Competing interests: The authors declare that they have no known competing financial interests or personal relationships that could have appeared to influence the work reported in this article.

Authors' Information

Abhishek Saxena received his bachelor's and master's degree in electrical engineering from RGPV Bhopal (State Technical University of M. P.), India, in 2012 and 2016, respectively. He is currently pursuing a Ph.D. degree from the National Institute of Technology, Patna, Bihar, India. His current research area includes demand response application in power systems for improved frequency regulation.

Ravi Shankar is currently working as an Assistant Professor in the Department of Electrical Engineering, National Institute of Technology Patna, India. He received his Ph.D. degree from the Indian Institute of Technology (Indian School of Mines) Dhanbad, India, in 2015. He has authored many research publications, which include journals of international repute, international and national conferences. His major research interests include soft computing techniques, artificial intelligent control design, flexible alternating current transmission system devices, renewable power, and energy storage application in power systems.

REFERENCES

[1] M. Ranjan and R. Shankar, "A literature survey on load frequency control considering renewable energy integration in power system: recent trends and future prospects," *Journal of Energy Storage*, vol. 45, Nov. 2022.

[2] G. Aydin, "The modeling of coal-related CO2 emissions and projections into future planning," *Energy Sources, Part A: Recovery, Utilization and Environmental Effects*, vol. 36, no. 2, pp. 191-201, Nov. 2013.

[3] I. Karakurt, G. Aydin, and S. Kaya *et al*., "Forecasting of Turkey's coal consumption using grey prediction technique," *Proceedings of the 24th International Mining Congress of Turkey, IMCET*, Apr. 2015, pp. 77-82.

[4] R. Choudhary, J. N. Rai, and Y. Arya, "FOPTID+1 controller with capacitive energy storage for AGC performance enrichment of multi-source Electric Power Systems," *Electric Power Systems Research*, vol. 221, pp. 109450, Aug. 2023.

[5] S. S. Khan, S. Ahmad, and M. Naeem, "On-grid joint energy management and trading in uncertain environment," *Applied Energy*, vol. 330, pp. 120318, Jan. 2023.

[6] D. Guha, P. K. Roy, and S. Banerjee, "Quasi-oppositional jaya optimized 2-degree-of-freedom PID controller for load-frequency control of Interconnected Power Systems," *International Journal of Modelling and Simulation*, vol. 42, no. 1, pp. 63-85, Oct. 2020.

[7] D. Guha, P. K. Roy, and S. Banerjee, "Optimal tuning of 3 degree-of-freedom proportional-integral-derivative controller for hybrid distributed power system using Dragonfly algorithm," *Computers & Electrical Engineering*, vol. 72, pp. 137-153, Nov. 2018.

[8] D. Guha, P. K. Roy, and S. Banerjee, "Disturbance observer aided optimised fractional-order three-degree-of-freedom tilt-integral-derivative controller for load frequency control of Power Systems," *IET Generation, Transmission & Distribution*, vol. 15, no. 4, pp. 716-736, Dec. 2020.

[9] A. D. Rosaline and U. Somarajan, "Structured H-infinity controller for an uncertain deregulated power system," *IEEE Transactions on Industry Applications*, vol. 55, no. 1, pp. 892-906, Jan. 2019.

[10] K. Singh and Y. Arya, "Tidal turbine support in microgrid frequency regulation through novel Cascade Fuzzy-FOPID Droop in de-loaded region," *ISA Transactions*, vol. 133, pp. 218-232, Feb. 2023.

[11] A. Anand, P. Aryan, and N. Kumari *et al*., "Type-2 fuzzy-based branched controller tuned using arithmetic optimizer for load frequency control," *Energy Sources, Part A: Recovery, Utilization, and Environmental Effects*, vol. 44, no. 2, pp. 4575-4596, May 2022.

[12] S. Biswas, P. K. Roy, and K. Chatterjee, "Development of MADB of P-I controller using LMI technique in a renewable energy based AGC system and study its application in a deregulated environment including energy storage device," *Optimal Control Applications and Methods*, vol. 44, no. 2, pp. 426-451, Aug. 2021.

[13] S. Batool, S. Ahmad, and A. Shoukat *et al*., "A data driven approach for optimal coordination of overcurrent Relay," in *2021 International Conference on Frontiers of Information Technology (FIT)*, Dec. 2021, pp. 90-95.

[14] S. Batool, S. Ahmad, and A. Shoukat *et al*., "Optimal coordination of overcurrent relay using rao-1 algorithm," in *2021 International Conference on Technology and Policy in Energy and Electric Power (ICT-PEP)*, Sep. 2021, pp. 15-162.

[15] N. R. Babu and L. C. Saikia, "Automatic generation control of a solar thermal and dish-stirling solar thermal system integrated multi-area system incorporating accurate HVDC link model using crow search algorithm optimised FOPI minus FODF controller," *IET Renewable Power Generation*, vol. 13, no. 12, pp. 2221-2231, Jul. 2019.

[16] S. M. Abd-Elazim and E. S. Ali, "Firefly algorithm-based load frequency controller design of a two area system composing of PV grid and thermal generator," *Electrical Engineering*, vol. 100, no. 2, pp. 1253-1262, Jun. 2017.

[17] S. Debbarma and A. Dutta, "Utilizing electric vehicles for LFC in restructured power systems using fractional order controller," *IEEE Transactions on Smart Grid*, vol. 8, no. 6, pp. 2554-2564, Nov. 2017.

[18] Y. Arya, "Effect of electric vehicles on load frequency control in interconnected thermal and hydrothermal power systems utilising CF-FOIDF controller," *IET Generation, Transmission & Distribution*, vol. 14, no. 14, pp. 2666-2675, May 2020.

[19] A. Saxena, R. Shankar, and S. K. Parida *et al*., "Demand response based optimally enhanced linear active disturbance rejection controller for Frequency Regulation in smart grid environment," *IEEE Transactions on Industry Applications*, vol. 58, no. 4, pp. 4337-4349, Jul. 2022.

[20] S. A. Hosseini, M. Toulabi, and A. Ashouri-Zadeh *et al*., "Battery energy storage systems and demand response applied to power system frequency control," *International Journal of Electrical Power & Energy Systems*, vol. 136, pp. 107680, Mar. 2022.

[21] S. R. Nayak, R. K. Khadanga, and Y. Arya *et al*., "Influence of ultra-capacitor on AGC of five-area hybrid power system with multi-type generations utilizing sine cosine adopted dingo optimization algorithm," *Electric Power Systems Research*, vol. 223, p. 109513, Oct. 2023.

[22] A. Latif, S. M. Hussain, and D. C. Das *et al*., "Double stage controller optimization for load frequency stabilization in hybrid wind-ocean wave energy based maritime microgrid system," *Applied Energy*, vol. 282, p. 116171, Jan. 2021.

[23] Y. Q. BAO, Y. LI, and B. WANG *et al*., "Demand response for frequency control of multi-area power system," *Journal of Modern Power Systems and Clean Energy*, vol. 5, no. 1, pp. 20-29, Jan. 2017.

[24] S. Mirjalili, "Salp swarm algorithm: a bio-inspired optimizer for engineering design problems," *Advances in Engineering Software*, vol. 114, pp. 163-191, Dec. 2017.

[25] S. Mirjalili and A. Lewis, "The whale optimization algorithm," *Advances in Engineering Software*, vol. 95, pp. 51-67, May 2016.

[26] D. Wang, D. Tan, and L. Liu, "Particle swarm optimization algorithm: an overview," *Soft Computing*, vol. 22, no. 2, pp. 387-408, Jan. 2017.

[27] S. Mirjalili, "The ant lion optimizer," *Advances in Engineering Software*, vol. 83, pp. 80-98, May 2015.

[28] S. Mirjalili, S. M. Mirjalili, and A. Lewis, "Grey wolf optimizer," *Advances in Engineering Software*, vol. 69, pp. 46-61, Mar. 2014.
[29] Z. Wu, W. Fu, and X. Ren, "Nonlinear inertia weighted Teaching-Learning-Based optimization for solving global optimization problem," *Computational Intelligence and Neuroscience*, vol. 2015, pp. 1-15, Jan. 2015.
[30] S. Mahdavi, S. Rahnamayan, and K. Deb, "Opposition based learning: a literature review," *Swarm and Evolutionary Computation (Print)*, vol. 39, pp. 1-23, Apr. 2018.
[31] A. A. Heidari, S. Mirjalili, and H. Faris *et al*., "Harris hawks optimization: algorithm and applications," *Future Generation Computer Systems*, vol. 97, pp. 849-872, Aug. 2019.
[32] J. Dai, Y. Liu, and C. Yan *et al*., "A coordinated control method of aggregate AC load for auxiliary frequency regulation service," *International Journal of Electrical Power & Energy Systems*, vol. 147, p. 108912, May 2023.
[33] S. A. Pourmousavi and M. H. Nehrir, "Introducing dynamic demand response in the LFC model," *IEEE Transactions on Power Systems*, vol. 29, no. 4, pp. 1562-1572, Jul. 2014.
[34] K. K. Bharti, V. P. Singh, and S. P. Singh, "Impact of intelligent demand response for load frequency control in smart grid perspective," *IETE Journal of Research*, vol. 68, no. 4, pp. 2433-2444, Jan. 2020.
[35] C. Pradhan, C. N. Bhende, and A. K. Srivastava, "Frequency sensitivity analysis of dynamic demand response in wind farm integrated power system," *IET Renewable Power Generation*, vol. 13, no. 6, pp. 905-919, Jan. 2019.
[36] P. Babahajiani, Q. Shafiee, and H. Bevrani, "Intelligent demand response contribution in frequency control of multi-area power systems," *IEEE Transactions on Smart Grid (Print)*, vol. 9, no. 2, pp. 1282-1291, Mar. 2018.
[37] S. A. Hosseini, M. Toulabi, and A. Ashouri-Zadeh *et al*., "Battery energy storage systems and demand response applied to power system frequency control," *International Journal of Electrical Power & Energy Systems*, vol. 136, p. 107680, Mar. 2022.
[38] J. Hu, J. Cao, and Y. Tang *et al*., "Demand response load following of source and load systems," *IEEE Transactions on Control Systems Technology (Print)*, vol. 25, no. 5, pp. 1586-1598, Sep. 2017.
[39] A. Aryandoust and J. Lilliestam, "The potential and usefulness of demand response to provide electricity system services," *Applied Energy*, vol. 204, pp. 749-766, Oct. 2017.
[40] C. K. Shiva, B. Vedik, and S. Mahapatra *et al*., "Load frequency stabilization of stand-alone hybrid distributed generation system using QOHS algorithm," *International Journal of Numerical Modelling: Electronic Networks, Devices and Fields*, vol. 35, no. 4, Mar. 2022.
[41] M. Nandi, C. K. Shiva, and V. Mukherjee, "TCSC based automatic generation control of deregulated power system using quasi-oppositional harmony search algorithm," *Engineering Science and Technology, an International Journal*, vol. 20, no. 4, pp. 1380-1395, Aug. 2017.
[42] R. Shankar, K. Chatterjee, and R. Bhushan, "Impact of energy storage system on load frequency control for diverse sources of interconnected power system in deregulated power environment," *International Journal of Electrical Power & Energy Systems*, vol. 79, pp. 11-26, Jul. 2016.
[43] A. Prakash, S. Murali, and R. Shankar *et al*., "HVDC tie-link modeling for restructured AGC using a novel fractional order cascade controller," *Electric Power Systems Research*, vol. 170, pp. 244-258, May 2019.
[44] A. Kumar and R. Shankar, "A quasi opposition Lion optimization algorithm for deregulated AGC considering hybrid energy storage system," *Journal of Electrical Engineering & Technology*, vol. 16, no. 6, pp. 2995-3015, Jul. 2021.
[45] M. R. Khalghani, J. Solanki, and S. K. Solanki *et al*., "Resilient frequency control design for microgrids under false data injection," *IEEE Transactions on Industrial Electronics*, vol. 68, no. 3, pp. 2151-2162, Mar. 2021.
[46] M. Khooban, T. Niknam, and M. Shasadeghi *et al*., "Load frequency control in microgrids based on a stochastic noninteger controller," *IEEE Transactions on Sustainable Energy*, vol. 9, no. 2, pp. 853-861, Apr. 2018.